DESIGN OPTIMIZATION OF ACOUSTIC METAMATERIALS AND PHONONIC CRYSTALS WITH A TIME DOMAIN METHOD

By

Weiyang Lin

James C. Newman III
Professor of Mechanical Engineering
(Chair)

W. Kyle Anderson
Professor (Retired)
(Co-Chair)

Kidambi Sreenivas
Research Professor
of Mechanical Engineering
(Committee Member)

Robert S. Webster
Research Associate Professor
of Mechanical Engineering
(Committee Member)

Boris Belinskiy
Professor of Mathematics
(Committee Member)

DESIGN OPTIMIZATION OF ACOUSTIC METAMATERIALS AND PHONONIC CRYSTALS WITH A TIME DOMAIN METHOD

By

Weiyang Lin

A Thesis Submitted to the Faculty of the University of
Tennessee at Chattanooga in Partial Fulfillment
of the Requirements of the Degree of
Doctor of Philosophy in Computational Engineering

The University of Tennessee at Chattanooga
Chattanooga, Tennessee

December 2016

ABSTRACT

A time-dependent adjoint approach for obtaining sensitivity derivatives for shape optimizations of acoustic metamaterials and phononic crystals is presented. The gradient-based design procedure is suitable for large numbers of design variables, and results are shown on achieving effective material properties with a unit cell and the broadband noise reduction with periodic arrays of cylinders. The acoustic wave propagation problem is solved in the time-domain using a Streamline Upwind/Petrov Galerkin formulation. Topology parameterization is accomplished using the homogenization method, and shape optimization is subsequently used afterwards to refine the geometries. Surface parameterization is accomplished using control grids, which are based on a Laplace equation. The combined strategy is compared with penalty-based topology optimization. Furthermore, the proposed topology optimization is also conducted on the design of a broadband acoustic cloaking device.

ACKNOWLEDGEMENTS

First, the author would like to thank his wife, Chao Wu, for encouragements during the work. It was her supports that made the author focus on the research and overcome the difficulties.

Many people have given great help in this project. The author would like to give special thanks to Drs. James Newman and Kyle Anderson for providing invaluable advice.

Last but not least, thanks are also given to the SimCenter for providing the author the academic training as well as the computational tools to complete the research for this project.

TABLE OF CONTENTS

LIST OF FIGURES

LIST OF ABBREVIATIONS

NRI: Negative refractive index

PDE: Partial differential equation

FEM: Finite element method

FVM: Finite volume method

DG: Discontinuous Galerkin formulation

SUPG: Streamline upwind Petrov Galerkin formulation

ncyc: Number of time steps in simulation

ndv: Number of design variables for optimization

SMI: Scaled material interpolation

TABLE OF SYMBOLS

p: Acoustic pressure

c: Speed of sound

Z: Impedance

n: Refractive index

$\mathbf{I}$: Cost function

β: Design variable

CHAPTER 1

INTRODUCTION

The feasibility of utilizing artificial materials with wave manipulating characteristics has been investigated for decades. Recently, metamaterials have raised significant interest because of their tremendous potential in many applications. By definition, metamaterials are engineered materials that have properties that cannot easily be found in nature. Such properties include negative refractive index, as shown in Fig. 1.1, as well as effective bulk modulus and mass density (Zhang 2010), and they can be applied for sound focusing (Guenneau et al. 2007), soundproofing, acoustic cloaking (Chen and Chan 2007; Cummer and Schurig 2007; Lin, Newman III, and Anderson 2016), and so on.

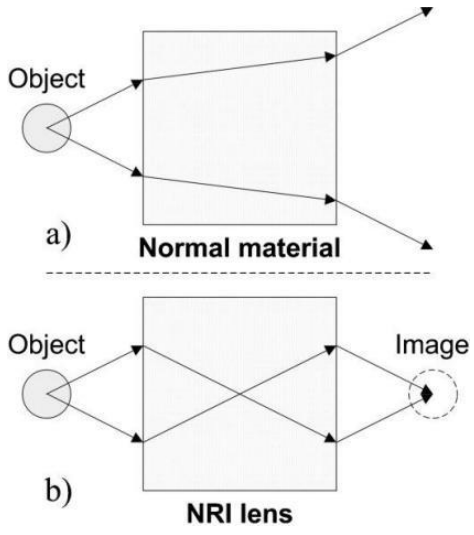

Figure 1.1 The concept of negative refractive index (NRI) (Pendry 2000)

Metamaterials are dedicated to sub-wavelength structures, and when the size of the design units increases, the target material behaves more like a phononic crystal where the macro arrangement becomes more important. Phononic crystals can be defined as periodic arrays of inclusions embedded in a host matrix. This kind of composite media is frequently designed to achieve the "phononic band-gap" which can be employed to prevent acoustic/elastic waves in certain frequencies from propagating (Liu et al. 2000). The phononic band structure of a phononic band gap crystal is conceptually similar to the electronic band structure of semiconductors. Applications include noise reductions, seismic shields (Alagoz and Alagoz 2009), waveguides, etc. More discussions of acoustic metamaterials and phononic crystals may be found in (Craster and Guenneau 2012; Deymier 2013).

Seeking an optimal structural pattern is usually accomplished by utilizing two categories of tools: shape and topology optimization. The shape optimization process begins with the parameterization of the original geometries and changes the parameters within allowable limits to achieve the minimization of an objective function. The resulting shapes are usually continuous and smooth. However, because shape parameterization is usually bound to certain types of changes, the magnitude of minimization of the objective function is limited (Lin, Anderson, et al. 2016).

Topology optimization treats geometries as if they are in a discrete domain (usually a Cartesian grid), and performs selections and de-selections of points based on the objective functional. This methodology is well suited for the overall design of materials and structures. Recently the level set method has become a popular method for topology optimizations. This method allows changes of the level set function based on the

sensitivity to obtain a desired distribution of materials as well as the overall shapes. Figure 1.2 shows an example of topologically optimized acoustic metamaterial for a given frequency using a level set-based method (Otomori et al. 2013). However, in practice these methods do not usually create new holes in material (Allaire and Jouve 2006). Another technique, referred to as the homogenization method, has been found to be robust in generating general layout of an optimal geometry (Bendsøe and Kikuchi 1988). The homogenization method has also been applied to the design of acoustic metamaterials (Diaz and Sigmund 2010; Lin, Newman, et al. 2016a). While proven successful, topology optimization is usually limited only to a conceptual level and typically requires adjustments to the final designs. Shape optimization is often employed along with topology optimizations for this purpose.

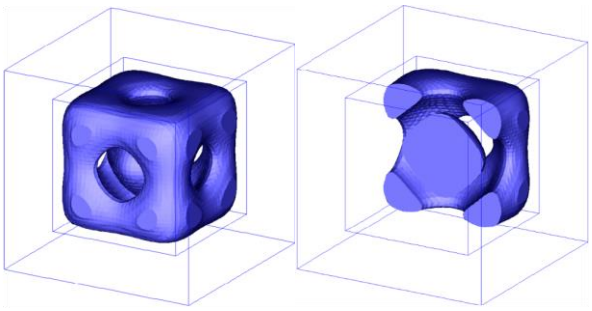

Figure 1.2 Optimization results of a 3D acoustic metamaterial targeting 5 kHz (Otomori et al. 2013)

Similar in both cases, gradient-based optimizers are used to minimize a specified objective function. While several techniques exist for evaluating the sensitivities derivatives for multidisciplinary simulations, the adjoint methods (Anderson and

Venkatakrishnan 1999) are of particular interest in this paper. For practical design, controls over various parts of the geometries are typically required, leading to a large number of design variables. The computational costs associated with an adjoint formulation scales with the number of cost function sensitivity derivatives and not the number of design variables. Therefore, the adjoint formulation is better suited for gradient-based design optimizations procedures that have large number of independent variables. However, for time-dependent sensitivity analysis, the adjoint formulation incurs additional costs associated with the time integration.

In this research, the shape and topology optimization of acoustic metamaterials and phononic crystals with time-dependent sensitivity analysis is presented. To achieve high-order accurate solutions and designs on continuous geometries, the Streamline Upwind/Petrov Galerkin time-domain method is utilized. Sensitivity analysis is conducted in order to perform the optimization, and an adjoint-based formulation is enabled when necessary. The optimization procedure is applied to periodic structures for broadband noise reduction, and a unit cell to achieve effective material properties. Additionally, the topology optimization is applied to an acoustic cloaking problem.

CHAPTER 2

FINITE ELEMENT TIME-DOMAIN FORMULATION

The simulations in this research is performed using a stabilized finite element method (Streamlined Upwind/Petrov Galerkin, or SUPG (Brooks and Hughes 1982)) for time-domain applications. Finite-difference time-domain (FDTD) methods have been widely adopted for solving different kinds of acoustic problems (Tam and Webb 1993; Botteldooren 1995). As the speed of computing resources increases and the need to represent the geometry with a conforming discretization becomes more of a concern, finite element methods (FEM) have become an alternative. While traditional finite-element time-domain (FETD) methods (Kallivokas and Bielak 1993) are used to solve for the second-order hyperbolic partial differential equations (PDEs), they have the disadvantage of resolving secondary variables with one order less accuracy than the primary variables. This problem can be overcome by a formulation based on the first-order governing PDEs recast from their second-order counterparts. A technique referred to as discontinuous Galerkin (DG) has recently been extended to acoustic problems based on the first-order PDEs (Käser and Dumbser 2006; Dumbser and Käser 2006). Both the SUPG and DG are the combination of finite volume methods (FVM) and FEM. They both have an origin in fluid mechanics (Cockburn and Shu 1998; Brooks and Hughes 1982), and are readily extended to nonlinear problems. It has been shown that SUPG has

the advantage of reduced number of unknowns in comparison with DG (Glasby et al. 2013).

2.1 Governing Equations and Transformations

In nature, primary waves (P-waves) of concern are compression waves that are longitudinal. In fluids, they take the form of acoustic waves. The physics of acoustic wave propagation, because of the nature of small-amplitude waves, can be modeled by linearizing the nonlinear Euler equations about some state. Because only small-amplitude motions are considered, an isotropic flow may be assumed, and the conservations of mass and momentum are sufficient to model the physics. Start with one-dimensional conservations laws

$$\frac{\partial Q_0}{\partial t} + \frac{\partial F_0}{\partial x} = 0 \tag{2.1}$$

where

$$Q_0 = \begin{bmatrix} \rho_0 \\ \rho_0 u_0 \end{bmatrix} \tag{2.2}$$

is the primary variables, ρ_0 is the density, u_0 is the velocity, and

$$F_0 = \begin{bmatrix} \rho_0 u_0 \\ \rho_0 u_0^2 + p_0 \end{bmatrix} \tag{2.3}$$

represents the fluxes of the respective components of Q_0, and p_0 is the static pressure. The primary variables can be expressed as

$$Q_0 = Q_e + Q \tag{2.4}$$

where Q_e is the background state and Q is the perturbation. Substituting into the Euler equations results in

$$\left[\frac{\partial Q_e}{\partial t}+\frac{\partial F_0}{\partial\left(Q_e+Q\right)}\frac{\partial Q_e}{\partial x}\right]+\left[\frac{\partial Q}{\partial t}+\frac{\partial F_0}{\partial\left(Q_e+Q\right)}\frac{\partial Q}{\partial x}\right]=0 \tag{2.5}$$

Since an acoustic wave is very small pressure disturbance that causes infinitesimal changes in density and pressure with infinitesimal values of velocity, the terms that involve powers or products of the *Q* variables may be discarded. Furthermore, since the terms in the first parenthesis satisfy the original Euler equations, Eq. (2.5) may be re-written as

$$\frac{\partial Q}{\partial t}+\frac{\partial F}{\partial Q_e}\frac{\partial Q}{\partial x}=0 \tag{2.6}$$

Following the derivation, the general three-dimensional acoustic wave propagation in a heterogeneous medium may be described by the equations

$$\frac{\partial p}{\partial t}+K_e\left(\frac{\partial u}{\partial x}+\frac{\partial v}{\partial y}+\frac{\partial w}{\partial z}\right)=0 \tag{2.7}$$

$$\frac{\partial u}{\partial t}+\frac{1}{\rho_e}\frac{\partial p}{\partial x}=0 \tag{2.8}$$

$$\frac{\partial v}{\partial t}+\frac{1}{\rho_e}\frac{\partial p}{\partial y}=0 \tag{2.9}$$

$$\frac{\partial w}{\partial t}+\frac{1}{\rho_e}\frac{\partial p}{\partial z}=0 \tag{2.10}$$

where p is the acoustic pressure, u, v and w are the velocity components. K_e is the bulk modulus of compressibility of the material, ρ_e is the density. The speed of sound can be obtained through the equation of state, and it may be evaluated as

$$c=\sqrt{\frac{K_e}{\rho_e}} \tag{2.11}$$

and the impedance may be calculated by

$$Z = \rho_e c \tag{2.12}$$

While acoustic wave equations are sufficient to describe wave propagation in fluids, elastic wave equations are typically employed for problems associated with solids to account for secondary waves (S-waves, shear waves) that are transverse (perpendicular) to the direction of propagation. More specifically, in solids, the bulk modulus of compressibility K_e is defined by

$$K_e = \lambda + \frac{2}{3}\mu \tag{2.13}$$

where λ and μ are the Lamé parameters characterizing the material, and μ is also called the shear modulus. Shear stresses are not supported in fluids (i.e. $\mu = 0$).

The general elastic wave equations may be written as (LeVeque 2002)

$$\frac{\partial \sigma_{xx}}{\partial t} - (\lambda + 2\mu)\frac{\partial u}{\partial x} - \lambda \frac{\partial v}{\partial y} - \lambda \frac{\partial w}{\partial z} = 0 \tag{2.14}$$

$$\frac{\partial \sigma_{yy}}{\partial t} - \lambda \frac{\partial u}{\partial x} - (\lambda + 2\mu)\frac{\partial v}{\partial y} - \lambda \frac{\partial w}{\partial z} = 0 \tag{2.15}$$

$$\frac{\partial \sigma_{zz}}{\partial t} - \lambda \frac{\partial u}{\partial x} - \lambda \frac{\partial v}{\partial y} - (\lambda + 2\mu)\frac{\partial w}{\partial z} = 0 \tag{2.16}$$

$$\frac{\partial \sigma_{xy}}{\partial t} - \mu\left(\frac{\partial v}{\partial x} + \frac{\partial u}{\partial y}\right) = 0 \tag{2.17}$$

$$\frac{\partial \sigma_{yz}}{\partial t} - \mu\left(\frac{\partial v}{\partial z} + \frac{\partial w}{\partial y}\right) = 0 \tag{2.18}$$

$$\frac{\partial \sigma_{xz}}{\partial t} - \mu\left(\frac{\partial u}{\partial z} + \frac{\partial w}{\partial x}\right) = 0 \tag{2.19}$$

$$\rho \frac{\partial u}{\partial t} - \frac{\partial \sigma_{xx}}{\partial x} - \frac{\partial \sigma_{xy}}{\partial y} - \frac{\partial \sigma_{xz}}{\partial z} = 0 \tag{2.20}$$

$$\rho \frac{\partial v}{\partial t} - \frac{\partial \sigma_{xy}}{\partial x} - \frac{\partial \sigma_{yy}}{\partial y} - \frac{\partial \sigma_{yz}}{\partial z} = 0 \tag{2.21}$$

$$\rho \frac{\partial w}{\partial t} - \frac{\partial \sigma_{xz}}{\partial x} - \frac{\partial \sigma_{yz}}{\partial y} - \frac{\partial \sigma_{zz}}{\partial z} = 0 \tag{2.22}$$

where σ_{xx}, σ_{yy} and σ_{zz} are the normal stress components, and σ_{xy}, σ_{xy} and σ_{yz} are the shear stress, u, v and w are the velocity components, ρ is the density of the material. The wave speeds are given by

$$c_p = \sqrt{\frac{\lambda + 2\mu}{\rho}} \tag{2.23}$$

for P-waves and

$$c_s = \sqrt{\frac{\mu}{\rho}} \tag{2.24}$$

for S-waves.

The governing equations in both cases can be written in a compact non-conservative form as

$$\frac{\partial Q}{\partial t} + A\frac{\partial Q}{\partial x} + B\frac{\partial Q}{\partial y} + C\frac{\partial Q}{\partial z} = 0 \tag{2.25}$$

where Q is the primitive variable vector, and A, B and C are functions of the material properties. When the material properties are constant across the elements, the spatial derivatives can be defined as

$$A\frac{\partial Q}{\partial x} + B\frac{\partial Q}{\partial y} + C\frac{\partial Q}{\partial z} = \nabla \cdot F \tag{2.26}$$

where

$$F = AQ\hat{i} + BQ\hat{j} + CQ\hat{k} \tag{2.27}$$

with $\hat{i}$, $\hat{j}$, $\hat{k}$ being unit vectors in the *x*, *y*, and *z* directions respectively.

The solution to the wave equations can be approximated by linear combinations of sinusoidal waves at various frequencies, which leads to a frequency-domain formulation for different time-harmonic sources. The time-domain solution is of interest in this research for its capability of solving broadband problems. Besides, in the time domain, the residual of the linear system is reduced several orders of magnitude, and requires much less search directions in a Krylov subspace (Anderson et al. 2011).

2.2 Stabilized Finite Element Formulation

In traditional finite element approaches, field variables are assumed continuous across element boundaries. The solution is assumed to vary within each element according to the superposition of a series of polynomial basis functions

$$Q_h = \sum_{i=1}^{np} N_i Q_i \tag{2.28}$$

where *np* is the number of modes determined by the degree of interpolation polynomials. Q_h represents the dependent variables approximated within each element, Q_i is the corresponding data at each node of the element, and each N_i represents a basis function. Popular choices of basis function include Lagrange polynomials, hierarchical basis functions (Wang and Mavriplis 2009), and Chebyshev polynomials (Wang 2002).

Finite element methods typically start with formulating the equations with a weighted residual method, which can be cast in the form of

$$\int_{\Omega} [\phi] \left(\frac{\partial Q}{\partial t} + A\frac{\partial Q}{\partial x} + B\frac{\partial Q}{\partial y} + C\frac{\partial Q}{\partial z} \right) \partial\Omega = 0 \tag{2.29}$$

where ϕ is a weighting function. Pioneered by Boris Grigorievich Galerkin, the Galerkin finite element method has become one of the most common finite element methods in simulation. In this method, the problem is formulated by selecting the set of weighting functions to be identical to the set of basis functions. This method, however, is known to give rise to central-difference type approximations of differential operators, which results in dispersive or wiggling solutions. The Streamlined Upwind Petrov-Galerkin (SUPG) method is introduced to stabilize the convective terms by the use of upwind differencing on the convective terms (Brooks and Hughes 1982). This can be done by adding a streamline upwind perturbation to the standard Galerkin weighting function. In the current research, the weighting function is adopted from Bonhaus (1998), given by

$$[\phi] = N[I] + \left(\frac{\partial N}{\partial x}[A] + \frac{\partial N}{\partial y}[B] + \frac{\partial N}{\partial z}[C] \right)[\tau] = N[I] + [P] \tag{2.30}$$

with

$$N = \sum_{i=1}^{np} N_i c_i \tag{2.31}$$

where c_i are arbitrary constants and $[\tau]$ is the stabilization matrix, which can be obtained using the following definitions

$$[\tau]^{-1} = \sum_{k=1}^{n} \left| \frac{\partial N_k}{\partial x}[A] + \frac{\partial N_k}{\partial y}[B] + \frac{\partial N_k}{\partial z}[C] \right| \tag{2.32}$$

where

$$\left| \frac{\partial N_k}{\partial x}[A] + \frac{\partial N_k}{\partial y}[B] + \frac{\partial N_k}{\partial z}[C] \right| = [T][|\Lambda|][T]^{-1} \tag{2.33}$$

Here, $[T]$ is right eigenvector matrix, and $[\Lambda]$ is a diagonal matrix whose entries are the eigenvalues, of the matrix on the left side. The inversion of local stabilization matrices $[\tau]$

can be calculated using Gauss eliminations.

Substituting the SUPG weighting function into the weighted residual form, and considering the fact that the solution is continuous within one material, the weak statement may be derived as

$$\int_{\Omega}\left[N\left\{\frac{\partial Q}{\partial t}\right\} - F\cdot\nabla N \right]\partial\Omega$$

$$+\int_{\Omega}[P]\left(\frac{\partial Q}{\partial t} + A\frac{\partial Q}{\partial x} + B\frac{\partial Q}{\partial y} + C\frac{\partial Q}{\partial z} \right)\partial\Omega \qquad (2.34)$$

$$+\int_{\Omega} N\left(A\frac{\partial Q}{\partial x} + B\frac{\partial Q}{\partial y} + C\frac{\partial Q}{\partial z} \right)\partial\Omega = 0$$

The third term can then be re-written as a surface integral using the divergence theorem

$$\int_{\Omega} N\left(A\frac{\partial Q}{\partial x} + B\frac{\partial Q}{\partial y} + C\frac{\partial Q}{\partial z} \right)\partial\Omega = \int_{\Gamma} NF\cdot\hat{n}\partial\Gamma \qquad (2.35)$$

The volume and surface integrals are evaluated using Gaussian quadrature rules. Since the set of basis functions is defined in standard elements such as isosceles right triangles, a coordinate mapping from the reference to a physical element is required for the computation of the first order derivatives and integrals. This transformation associated with element *k* may be written as

$$\begin{bmatrix} x_k \\ y_k \\ z_k \end{bmatrix} = \sum_{i=1}^{np} \begin{bmatrix} \tilde{x}_{k,i} \\ \tilde{y}_{k,i} \\ \tilde{z}_{k,i} \end{bmatrix} N_i(\xi,\eta,\zeta) \qquad (2.36)$$

where (x, y, z) are the physical coordinates, and (ξ, η, ζ) represent the coordinates in the reference element. The corresponding Jacobian J_k is given by

$$J_k = \begin{bmatrix} \frac{\partial x}{\partial \xi} & \frac{\partial x}{\partial \eta} & \frac{\partial x}{\partial \zeta} \\ \frac{\partial y}{\partial \xi} & \frac{\partial y}{\partial \eta} & \frac{\partial y}{\partial \zeta} \\ \frac{\partial z}{\partial \xi} & \frac{\partial z}{\partial \eta} & \frac{\partial z}{\partial \zeta} \end{bmatrix} \tag{2.37}$$

The integrals can be approximated by applying the Gaussian quadrature rules with weights w_i as

$$\int_\Omega f\left(x,y,z\right) d\Omega \cong \frac{1}{2} \sum_{i=1}^{ngauss} f\left(\xi_i,\eta_i,\zeta_i\right) w_i \det\left(J_i\right) \tag{2.38}$$

When the dependent variable is represented by a polynomial basis of order p, volume integrals are evaluated using formulas that will exactly integrate polynomials of order $2p$ and surface integrals of order $2p+1$. The surface integrals in the interior of the domain do not need to be evaluated due to the use of a Galerkin formulation.

The temporal discretization of the governing equation is advanced by implementing a backward differentiation formula (BDF). For each time step k, the BDF1 and BDF2 schemes may be expressed as

$$Q^k - Q^{k-1} = \Delta t \frac{\partial Q^k}{\partial t} \tag{2.39}$$

and

$$Q^k - \frac{4}{3} Q^{k-1} + \frac{1}{3} Q^{k-2} = \frac{2}{3} \Delta t \frac{\partial Q^k}{\partial t} \tag{2.40}$$

The solution is obtained with an implicit time marching approach. At each time step, the generalized minimal residual (GMRES) linear system equation solver (Saad and Schultz 1986) is utilized with an incomplete lower-upper (ILU) preconditioner (Saad

2003) to solve for the non-diagonally dominant system as a result of the finite element formulation.

2.3 Acoustic Metamaterials and Phononic Crystals

On the boundaries of the physical domain, the appropriate boundary conditions are strongly enforced by incorporating them into the surface integral. At the interfaces of different materials, the surface integral must be evaluated because of the discontinuous jump of material properties. As shown in Fig. 2.1, duplicate faces are created at the interfaces to accurately capture the jump conditions, which leads to a hybrid continuous/discontinuous Galerkin formulation. Spurious solutions are precluded with this treatment (Anderson et al. 2011). A Godunov flux formulation is used to model the Riemann problem (LeVeque 2002). In this formulation, the fluxes across the interface are given by

$$\Phi_L = F\left(Q_L\right)\hat{n} + A^{-}\Delta Q \tag{2.41}$$

for the left cell, and

$$\Phi_R = F\left(Q_R\right)\hat{n} - A^{+}\Delta Q \tag{2.42}$$

for the right cell, where $A^{-} = R\Lambda^{-}R^{-1}$ and $A^{+} = R\Lambda^{+}R^{-1}$, and they are evaluated by either averaging the two states or a special average suggested by LeVeque (2002). For example, the averaging matrices for acoustic equations are given by

$$A^{+,-}=\begin{bmatrix} -\frac{c^{+,-}}{2} & \frac{n_x K_e^{+,-}}{2} & \frac{n_y K_e^{+,-}}{2} & \frac{n_z K_e^{+,-}}{2} \\ -\frac{n_x}{2\rho_e^{+,-}} & -\frac{n_x^2 c^{+,-}}{2} & -\frac{n_x n_y c^{+,-}}{2} & -\frac{n_x n_z c^{+,-}}{2} \\ \frac{n_y}{2\rho_e^{+,-}} & -\frac{n_y n_x c^{+,-}}{2} & -\frac{n_y^2 c^{+,-}}{2} & -\frac{n_y n_z c^{+,-}}{2} \\ \frac{n_z}{2\rho_e^{+,-}} & -\frac{n_z n_x c^{+,-}}{2} & -\frac{n_z n_y c^{+,-}}{2} & -\frac{n_z^2 c^{+,-}}{2} \end{bmatrix} \tag{2.43}$$

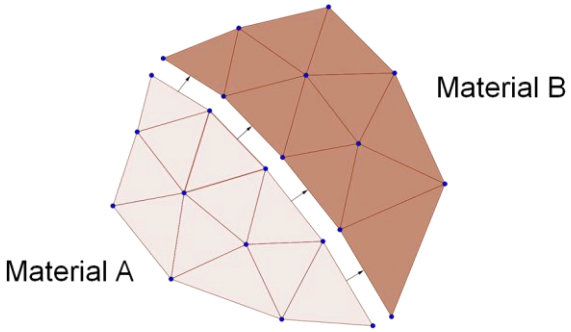

Figure 2.1 Duplicate faces used to model the multi-material problem

Duplicate faces are also created to approximate periodic boundary conditions. Because of the nature of periodicity of phononic crystals, a general periodic boundary condition is needed to model this property so that the simulation may be conducted in a single lattice, as shown in Fig. 2.2. More specifically, the equation

$$Q(r)=Q(r+r_p) \tag{2.44}$$

has to be satisfied, where r_p is any linear combination of the primitive lattice vector as indicated in Fig. 2.2 (Joannopoulos et al. 2011). By applying Bloch's theorem (Brillouin 2003) to the example of a 2D crystal in Fig. 2.2, the modes of the crystal may be

characterized by

$$Q(r) = e^{ik \cdot r} Q(r + r_p) \tag{2.45}$$

where k is the wave vector in the Brillouin zone. A properly designed single lattice may exhibit a complete band gap that covers all possible propagation directions that correspond to the wave vectors in the first Brillouin zone, as shown in light blue color in Fig. 2.2. In practice, the general periodic boundary condition may be implemented by solving the Riemann's problem at the duplicate faces with values associated with the complex multiplier e^{ikr}.

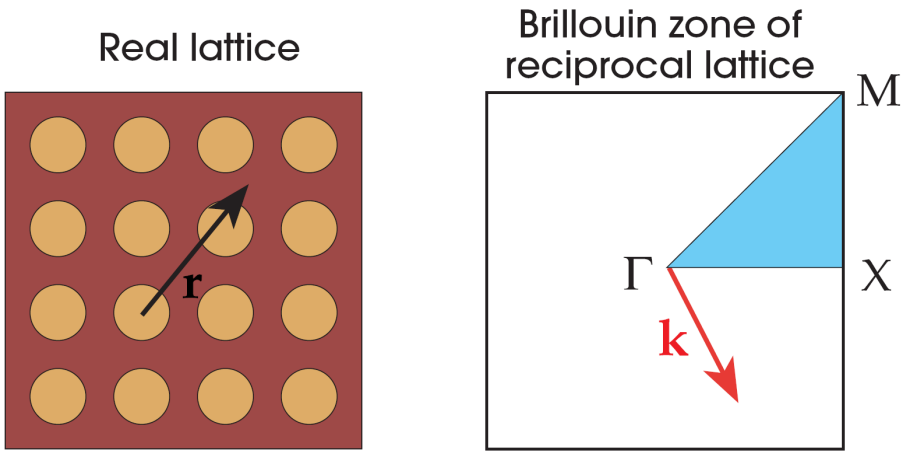

Figure 2.2 A 2D photonic crystal and the Brillouin zone (Joannopoulos et al. 2011)

In simulation problems of acoustic metamaterials and phononic crystals, the frequency domain solutions are usually of interest. Frequency domain solutions can be obtained by conducting a Fourier transformation of the time domain solution, and to obtain time domain solutions from frequency domain solutions, an inverse Fourier

transformation may be employed. The discrete Fourier transformation on the time domain solution may be approximated as

$$\hat{Q}_j = \sum_{k=1}^{ncyc} Q^k \phi_j^k \tag{2.46}$$

where

$$\phi_j = \exp\left(-i \cdot 2\pi\omega_j t\right)\Delta t \tag{2.47}$$

and $\hat{Q}_j$ represents the frequency domain solution at frequency ω_j . Besides, *ncyc* represents the total number of time steps (cycles). The simulations are usually conducted till the frequency domain solutions are converged to a certain tolerance.

2.4 Parallel Implementation on Distributed Memory Machines

The proposed finite element solver is implemented for a distributed memory space using message passing interface (MPI). To utilize the parallel computational resources, the global computational mesh needs to be decomposed into subdomains. Overlapping nodes (ghost nodes) are created at the subdomain interfaces for information exchange among processes, as shown in Fig. 2.3.

The partitioning of computational meshes is efficiently carried out by METIS (Karypis and Kumar 1995), such that the surface-to-volume ratio is minimized, leading to an optimized parallel computation. An example of domain decomposition is shown in Fig. 2.4.

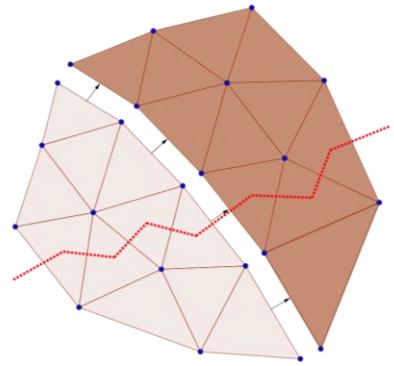

(a) Arbitrary domain decomposition by the red line

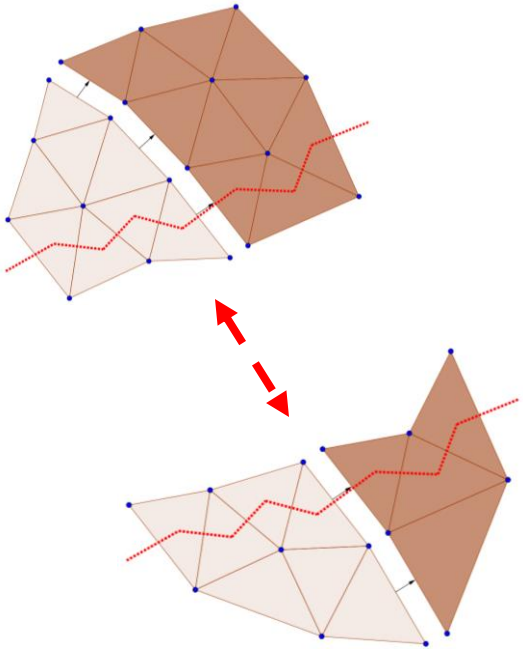

(b) Decomposed subdomains

Figure 2.3 An example of the domain decomposition with ghost nodes for communication

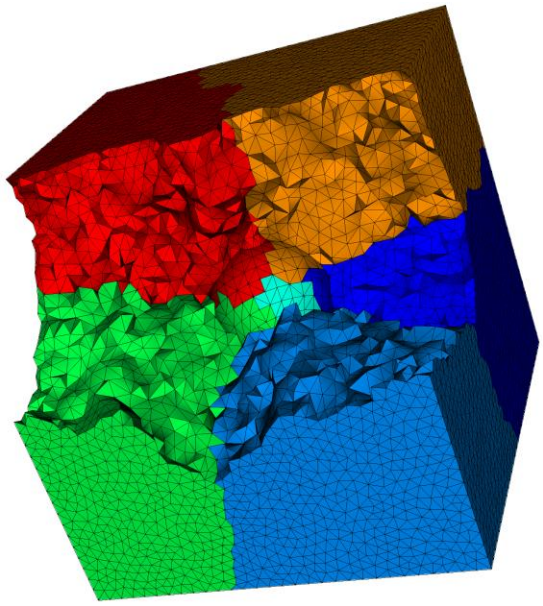

Figure 2.4 An example of 3D domain decomposition using METIS.

CHAPTER 3

SENSITIVITY ANALYSIS AND DESIGN METHODOLOGIES

In gradient-based optimization frameworks, a functional **I** to be minimized is typically described with a set of design variables β. Depending on the application, the cost function can be the, for example, transmitted or reflected pressure at a specified location, pressure at a given frequency, or a combination of different physical quantities. The sensitivity derivatives of the functional (i.e., the cost function) with respect to the design variables are utilized to evaluate an appropriate search direction for improving the design.

3.1 Sensitivity Analysis for Time-Dependent Problems

The sensitivity derivatives, or the gradients of the cost function with respect to the design variables, may be calculated in many different ways. The most straightforward method may be the finite-difference method, where a central-difference is given by

$$\frac{\mathrm{d}\mathbf{I}}{\mathrm{d}\beta} = \frac{\mathbf{I}\left(\beta + \Delta\beta\right) - \mathbf{I}\left(\beta - \Delta\beta\right)}{2\Delta\beta} + O\left(\Delta\beta^2\right) \tag{3.1}$$

However, this method suffers from inaccuracy because of step-size problems and is usually prohibitively expensive. Another way to approximate the derivatives is through the use of complex Taylor series expansion (CTSE). This method perturbs the design variables in the complex part, resulting in higher-accuracy than finite-difference methods because of the elimination of subtractive cancellation error (Newman III et al. 1999;

Anderson et al. 2001)

$$\frac{\mathrm{d}\mathbf{I}}{\mathrm{d}\beta} = \frac{\mathrm{Im}\left[\mathbf{I}\left(\beta + \Delta\beta i\right)\right]}{\Delta\beta} + O\left(\Delta\beta^2\right) \tag{3.2}$$

However, similar to the finite-difference methods, CTSE is generally too expensive to have practical implementations because of the requirement of multiple function evaluations.

Alternatively, the sensitivity derivative can be computed using a forward mode direct differentiation by examining the functional dependencies of the cost function. Since the cost function is defined by a functional with dependencies on the design variables β, arbitrary dependent variable D, and the solution quantities Q, i.e.,

$$\mathbf{I} = \mathbf{I}\left(\beta, D, Q\right) \tag{3.3}$$

the total differential of I with respect to β can be expressed by

$$\frac{\mathrm{d}\mathbf{I}}{\mathrm{d}\beta} = \frac{\partial\mathbf{I}}{\partial\beta} + \frac{\partial\mathbf{I}}{\partial D}\frac{\partial D}{\partial\beta} + \frac{\partial\mathbf{I}}{\partial Q}\frac{\partial Q}{\partial\beta} \tag{3.4}$$

The residual of the governing equation for a steady problem may be expressed as

$$R\left(\beta, D, Q\right) = 0 \tag{3.5}$$

then the total differential of R with respect to β is given by

$$\frac{\mathrm{d}R}{\mathrm{d}\beta} = \frac{\partial R}{\partial\beta} + \frac{\partial R}{\partial D}\frac{\partial D}{\partial\beta} + \frac{\partial R}{\partial Q}\frac{\partial Q}{\partial\beta} = 0 \tag{3.6}$$

In some applications, the residual is not an explicit function of β, thus Eq. (14) may be rewritten in the form of the solution sensitivity

$$\frac{\partial Q}{\partial\beta} = -\left[\frac{\partial R}{\partial Q}\right]^{-1}\left(\frac{\partial R}{\partial D}\frac{\partial D}{\partial\beta}\right) \tag{3.7}$$

Substituting back into Eq. (3.4), the sensitivity derivative becomes

$$\frac{\mathrm{d}\mathbf{I}}{\mathrm{d}\beta} = \frac{\partial \mathbf{I}}{\partial \beta} + \frac{\partial \mathbf{I}}{\partial D}\frac{\partial D}{\partial \beta} - \frac{\partial \mathbf{I}}{\partial Q}\left[\frac{\partial R}{\partial Q}\right]^{-1}\left(\frac{\partial R}{\partial D}\frac{\partial D}{\partial \beta}\right) \tag{3.8}$$

In time-dependent problems such as transient acoustics, the solutions from the previous time-steps have to be considered in the calculation of the residual of the governing equation. For a backward differentiation formula, BDF2 in this case, the total differential of R with respect to β at time-step k is expanded to

$$R^k\left(\beta, D, Q^k, Q^{k-1}, Q^{k-2}\right) = 0 \tag{3.9}$$

and therefore the total differential of R^k with respect to β becomes

$$\frac{\mathrm{d}R^k}{\mathrm{d}\beta} = \frac{\partial R^k}{\partial \beta} + \frac{\partial R^k}{\partial D}\frac{\partial D}{\partial \beta} + \frac{\partial R^k}{\partial Q^k}\frac{\partial Q^k}{\partial \beta} + \frac{\partial R^k}{\partial Q^{k-1}}\frac{\partial Q^{k-1}}{\partial \beta} + \frac{\partial R^k}{\partial Q^{k-2}}\frac{\partial Q^{k-2}}{\partial \beta} = 0 \tag{3.10}$$

Again if the residual is not an explicit function of β, Eq. (3.10) may be rewritten as

$$\frac{\partial Q^k}{\partial \beta} = -\left[\frac{\partial R^k}{\partial Q^k}\right]^{-1}\left(\frac{\partial R^k}{\partial D}\frac{\partial D}{\partial \beta} + \frac{\partial R^k}{\partial Q^{k-1}}\frac{\partial Q^{k-1}}{\partial \beta} + \frac{\partial R^k}{\partial Q^{k-2}}\frac{\partial Q^{k-2}}{\partial \beta}\right) \tag{3.11}$$

Substituting it back into Eq. (3.4) results in the sensitivity derivative for time-dependent problems using the forward mode, and notice the sensitivity of cost function **I** with respect to each Q^k needs to be integrated in time

$$\frac{\mathrm{d}\mathbf{I}}{\mathrm{d}\beta} = \frac{\partial \mathbf{I}}{\partial \beta} + \frac{\partial \mathbf{I}}{\partial D}\frac{\partial D}{\partial \beta}$$

$$-\sum_{k=1}^{ncyc}\frac{\partial \mathbf{I}}{\partial Q^k}\left[\frac{\partial R^k}{\partial Q^k}\right]^{-1}\left(\frac{\partial R^k}{\partial D}\frac{\partial D}{\partial \beta} + \frac{\partial R^k}{\partial Q^{k-1}}\frac{\partial Q^{k-1}}{\partial \beta} + \frac{\partial R^k}{\partial Q^{k-2}}\frac{\partial Q^{k-2}}{\partial \beta}\right) \tag{3.12}$$

As seen from Eq. (3.12), the computational costs for the forward mode scale with the number of design variables.

3.2 Adjoint Formulation for Time-Dependent Problems

As the number of design variables increases, the implementation of an adjoint method for computing sensitivity derivatives becomes the more efficient formulation. Examining Eq. (3.12), it is found that the additional computational overhead is due to the repetitive calculations of the solution sensitivities in Eq. (3.11). The adjoint methodology eliminates this overhead by transposing the inverse of the Jacobian matrix

$$\frac{\mathrm{d}\mathbf{I}}{\mathrm{d}\beta} = \frac{\partial \mathbf{I}}{\partial \beta} + \frac{\partial \mathbf{I}}{\partial D}\frac{\partial D}{\partial \beta} - \left[\left[\frac{\partial R}{\partial Q}\right]^{-T}\left[\frac{\partial \mathbf{I}}{\partial Q}\right]^{T}\right]^{T}\left(\frac{\partial R}{\partial D}\frac{\partial D}{\partial \beta}\right) \tag{3.13}$$

and by defining the adjoint variable

$$\lambda_Q = -\left[\frac{\partial R}{\partial Q}\right]^{-T}\left[\frac{\partial \mathbf{I}}{\partial Q}\right]^{T} \tag{3.14}$$

Utilizing Eq. (3.14), the resulting final form of the adjoint equation for steady-state problems becomes

$$\frac{\mathrm{d}\mathbf{I}}{\mathrm{d}\beta} = \frac{\partial \mathbf{I}}{\partial \beta} + \frac{\partial \mathbf{I}}{\partial D}\frac{\partial D}{\partial \beta} + \lambda_Q^T\left(\frac{\partial R}{\partial D}\frac{\partial D}{\partial \beta}\right) \tag{3.15}$$

The adjoint-based formulation is more complex for time-dependent problems. Similar to the steady-state case, it is derived by transposing the inverse of the Jacobian matrices. Examine the third term in Eq. (3.12),

$$\sum_{k=1}^{ncyc}\frac{\partial \mathbf{I}}{\partial Q^k}\left[\frac{\partial R^k}{\partial Q^k}\right]^{-1}\left(\frac{\partial R^k}{\partial D}\frac{\partial D}{\partial \beta} + \frac{\partial R^k}{\partial Q^{k-1}}\frac{\partial Q^{k-1}}{\partial \beta} + \frac{\partial R^k}{\partial Q^{k-2}}\frac{\partial Q^{k-2}}{\partial \beta}\right)$$

$$= \sum_{k=1}^{ncyc}\left[\lambda_Q^k\right]^T\left(\frac{\partial R^k}{\partial D}\frac{\partial D}{\partial \beta} + \frac{\partial R^k}{\partial Q^{k-1}}\frac{\partial Q^{k-1}}{\partial \beta} + \frac{\partial R^k}{\partial Q^{k-2}}\frac{\partial Q^{k-2}}{\partial \beta}\right)$$

$$= \sum_{k=1}^{ncyc} \left(\left[\lambda_Q^k \right]^T \frac{\partial R^k}{\partial D} \frac{\partial D}{\partial \beta} + \left[\psi_1^k \right]^T \frac{\partial Q^{k-1}}{\partial \beta} + \left[\psi_2^k \right]^T \frac{\partial Q^{k-2}}{\partial \beta} \right) \tag{3.16}$$

where

$$\lambda_Q^k = \left[\frac{\partial R^k}{\partial Q^k} \right]^{-T} \left[\frac{\partial \mathbf{I}}{\partial Q^k} \right]^T \tag{3.17}$$

$$\psi_1^k = \left[\frac{\partial R^k}{\partial Q^{k-1}} \right]^T \lambda_Q^k \tag{3.18}$$

$$\psi_2^k = \left[\frac{\partial R^k}{\partial Q^{k-2}} \right]^T \lambda_Q^k \tag{3.19}$$

It is observed from Eq. (3.16) that the evaluation of each term involves the solution sensitivities from the earlier two time-steps, which are unfortunately not readily available. To overcome this problem, the adjoint variables of "newer" time-steps can be regrouped with the ones of "older" time-steps; that is, the adjoint variable is reformulated as

$$\lambda_Q^k = \left[\frac{\partial R^k}{\partial Q^k} \right]^{-T} \left(\left[\frac{\partial \mathbf{I}}{\partial Q^k} \right]^T + \left[\psi_1^{k+1} \right]^T + \left[\psi_2^{k+2} \right]^T \right) \tag{3.20}$$

The basic algorithm can thus be written as

Algorithm. A discrete adjoint formulation for time-dependent sensitivity derivatives

1. Set ψ_1^{k+1}, ψ_2^{k+1} and ψ_2^{k+2} to be zero. Set *k* to be *ncyc* (number of time steps)
2. Solve Eq. (3.20) for the adjoint variable.
3. Set the sensitivity derivatives by

$$\frac{\mathrm{d}\mathbf{I}}{\mathrm{d}\beta} = \frac{\mathrm{d}\mathbf{I}}{\mathrm{d}\beta} + \left[\lambda_Q^k \right]^T \frac{\partial R^k}{\partial D} \frac{\partial D}{\partial \beta} + \frac{\partial \mathbf{I}}{\partial D} \frac{\partial D}{\partial \beta} \tag{3.21}$$

4. Set $k = k - 1$.

5. Set $\psi_2^{k+2} = \psi_2^{k+1}$, solve Eqs. (3.18-3.19) for ψ_1^{k+1} and ψ_2^{k+1}.

6. If $k = 1$, stop; otherwise go to step 2.

In general, adjoint formulation requires the storage of sensitivity matrices for all time steps for nonlinear problems because of the change of Jacobian matrices. For large-scale problems, this becomes prohibitive. The storage problem can be mitigated by an approximate formulation of this algorithm. By dividing the global time into several intervals, local-in-time sensitivities can be calculated, and the sum of the local sensitivities is found to be an approximation to the global sensitivities (Yamaleev, Diskin, and Nielsen 2010; Lin, Anderson, et al. 2016).

3.3 Adjoint Formulation for Frequency Domain Solutions

Consider a special case where the cost function **I** is defined as

$$\mathbf{I} = \sum_{j=1}^{nfreq} \hat{Q}_j \overline{\hat{Q}_j} \tag{3.22}$$

where $\overline{\hat{Q}_j}$ is the complex conjugate of $\hat{Q}_j$, which is the frequency domain solution as in Eqs. (2.46-2.47). The sensitivity of the cost function with respect to time dependent solution Q^k may be expressed as

$$\frac{\mathrm{d}\mathbf{I}}{\mathrm{d}Q^k} = \sum_{j=1}^{nfreq} \left[\overline{\hat{Q}_j} \phi_j^k + \hat{Q}_j \phi_j^{-k} \right] \tag{3.23}$$

Note that the frequency domain solution $\hat{Q}_j$ is ready for use since it is obtained before the adjoint sensitivity calculation.

In a typical acoustics application, the transmittance T and reflectance R are collected by integrating the values on certain boundaries. Suppose the cost function **I** has

dependencies upon *T* and *R*, for example,

$$\mathbf{I} = \sum_{j=1}^{nfreq} \mathbf{I}_k \left(\hat{T}_k, \hat{R}_k \right) \tag{3.24}$$

where $\left(\hat{T}_k, \hat{R}_k \right)$ are the frequency domain solutions based on $\left(T, R \right)$. Similarly, the sensitivity of the cost function with respect to time dependent solution Q^k may be expressed as

$$\frac{\mathrm{d}\mathbf{I}}{\mathrm{d}Q^k} = \sum_{j=1}^{nfreq} \left(\frac{\partial \mathbf{I}_k}{\partial \hat{R}_k} \frac{\partial \hat{R}_k}{\partial R} \frac{\partial R}{\partial Q^k} + \frac{\partial \mathbf{I}_k}{\partial \hat{T}_k} \frac{\partial \hat{T}_k}{\partial T} \frac{\partial T}{\partial Q^k} \right) \tag{3.25}$$

which can be regrouped as

$$\frac{\mathrm{d}\mathbf{I}}{\mathrm{d}Q^k} = \left[\sum_{j=1}^{nfreq} \left(\frac{\partial \mathbf{I}_k}{\partial \hat{R}_k} \frac{\partial \hat{R}_k}{\partial R} \right) \right] \frac{\partial R}{\partial Q^k} + \left[\sum_{j=1}^{nfreq} \left(\frac{\partial \mathbf{I}_k}{\partial \hat{T}_k} \frac{\partial \hat{T}_k}{\partial T} \right) \right] \frac{\partial T}{\partial Q^k} \tag{3.26}$$

for implementation.

3.4 Shape Parameterization and Sensitivity Derivatives

An important step in the framework of shape optimization is the method used to describe the geometries of interest. A number of surface parameterization methods have been developed by researchers, including the use of the individual mesh points on the surface of the mesh, Bezier, B-spline, and nonuniform rational B-spline (NURBS) surfaces, Hicks-Henne functions, sine functions, discipline specific functions, basis vectors, and free-form deformation.

The surface can be parameterized using a modified Hicks-Henne bump function (Hicks and Henne 1978), which can be extended to two-dimensional surfaces

$$b_i = \sin^4 \left(\pi x^{m_i} \right) \sin^4 \left(\pi y^{n_i} \right) \tag{3.27}$$

with

$$m_i = \frac{\ln(0.5)}{\ln\left(x_{M_i}\right)} \tag{3.28}$$

$$n_i = \frac{\ln(0.5)}{\ln\left(y_{N_i}\right)} \tag{3.29}$$

where x and y are the coordinates on the surface, and x_{M_i} and y_{N_i} are pre-selected values corresponding to the locations of the maxima. To ensure the clustering at the end points, the locations of x_{M_i} and y_{N_i} are selected appropriately. For example, selecting

$$x_{M_i} = 0.5 \cdot \left[1 - \cos\left(\theta_i\right)\right] \tag{3.30}$$

achieves the desired clustering, where $\theta_i = \pi \cdot i / (N+1)$, and N is the number of control points. However, x_{M_i} can also be chosen to be the same as θ_i such that the control points are equally spaced. Figure 3.1 shows the shapes of the modified Hicks-Henne functions for a given domain.

The weights of these shape functions b_i are considered the design variables, which yields the calculation of the displacement in the direction of wave propagation as

$$\Delta z_n = \sum_{i=1}^{ndv} \beta_i \cdot b_i\left(x_n, y_n\right) \tag{3.31}$$

The deformation with randomly chosen design variables is shown in Fig. 3.2 for illustrative purposes. The derivatives of the parameterization are given by

$$\frac{\partial z_n}{\partial \beta_i} = b_i\left(x_n, y_n\right) \tag{3.32}$$

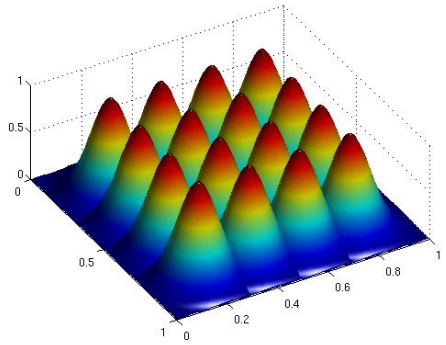

Figure 3.1 Modified Hicks-Henne bump functions for surface deformations.

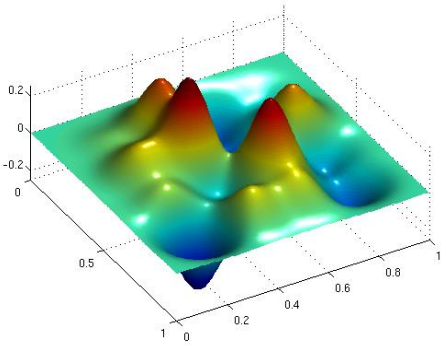

Figure 3.2 Sample illustration of a surface deformation with the modified Hicks-Henne bump functions and randomly generated design variables.

Another technique, referred to as control grids, is also used in this research due to its advantages in multidisciplinary applications (Anderson, Karman, and Burdyshaw 2009). In this method, the design variables are specified at the user-defined locations of control geometry. A Laplace equation is then solved for each perturbation direction using the design variables as Dirichlet boundary conditions as

$$\nabla^2 \delta_x = 0 \tag{3.33}$$

$$\nabla^2 \delta_y = 0 \tag{3.34}$$

$$\nabla^2 \delta_z = 0 \tag{3.35}$$

$$\delta_x, \delta_y, \delta_z = f(\beta) \text{ on } \Gamma \tag{3.36}$$

The equations are discretized using commonly used finite-difference formulas, and a successive over-relaxation method can be used to solve for the solution. The coordinates of each mesh point (x, y, z) may be updated by adding the associated perturbations to the original coordinates (x^0, y^0, z^0) after the solutions are obtained as

$$x = x^0 + \delta_x \tag{3.37}$$

$$y = y^0 + \delta_y \tag{3.38}$$

$$z = z^0 + \delta_z \tag{3.39}$$

An important feature of the control grids is that, since a linear partial differential equation is used and the perturbation is always added to the original geometry, these solutions only need to be done once and the results saved in a table, G; thus, the coordinates of the deformed boundaries may be written as

$$X_B = X_B^0 + \sum_{i=1}^{ndv} \beta_i G_i \tag{3.40}$$

where X_B^0 represents the original shape (x^0, y^0, z^0) and X_B is after deformation (x, y, z). An example of the application of control grids on a 2D unit cell is shown in Figs. 3.3 and 3.4, and the contours show the magnitude of the solution to the Laplace equations. In this example, the volume ratio is 0.274 and 16 design variables are used to control the deformation of the inclusion. This technique can also be applied to three dimensional geometries. Figures 3.5 and 3.6 show the solutions to the Laplace equations, with which the original geometry in Fig. 3.7 is deformed, as shown in Fig. 3.8.

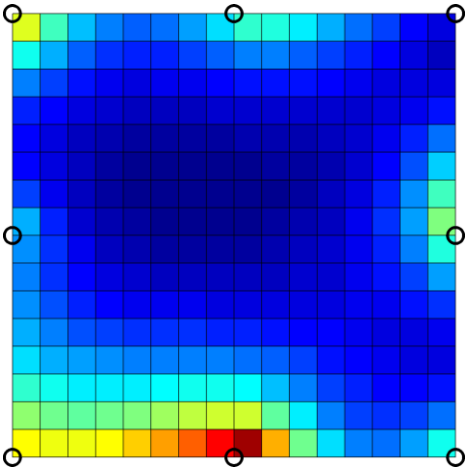

Figure 3.3 Control grid including the depiction of points on the design grid surface

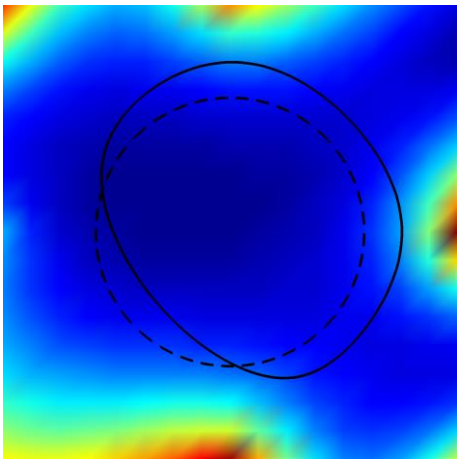

Figure 3.4 An example showing the original (dashed line) and the deformed (solid line) shapes for a single unit cell of periodic structures

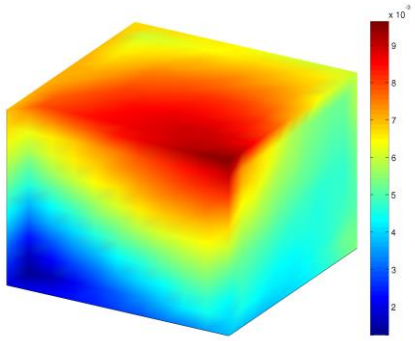

Figure 3.5 Control grid with perturbation field on the surface.

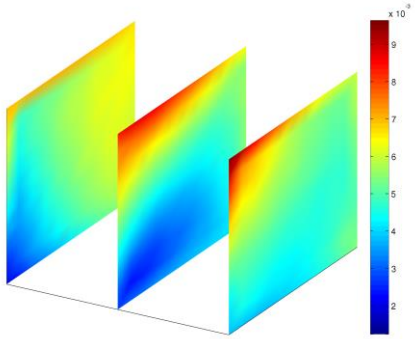

Figure 3.6 Slices of control grid with perturbation field.

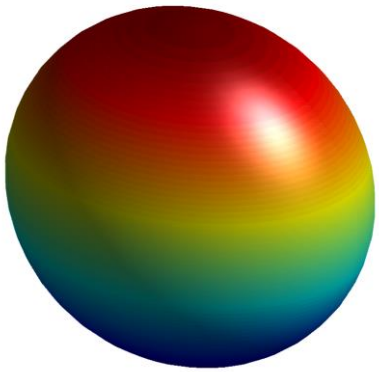

Figure 3.7 The original shape of a sphere.

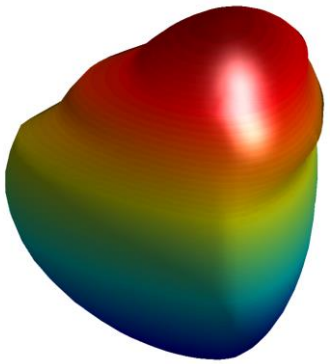

Figure 3.8 The deformed shape based on the perturbation field obtained by control grid.

In shape optimization, the arbitrary dependent variable D is chosen to be the resulting deformation of the computational mesh X

$$D = X \tag{3.41}$$

The mesh sensitivities generally require the sensitivity derivatives of the surface mesh points with respect to the design variables and may be expressed as

$$\frac{\partial X}{\partial \beta} = \left[K\right]^{-1} \frac{\partial X_B}{\partial \beta} \tag{3.42}$$

where X_B is the deformation on the surfaces and $[K]$ is the stiffness matrix for solving the resulting mesh movement X as the deformations are propagated into the interior using linear elasticity.

When the mesh movement derivatives of Eq. (3.37) are substituted into the sensitivity derivatives Eq. (3.15), it is realized that the calculation may be further reduced

by introducing another adjoint variable λ_X (Nielsen and Park 2006). For example, the steady-state adjoint formulation given in Eq. (3.15) can now be re-written as

$$\frac{\mathrm{d}\mathbf{I}}{\mathrm{d}\beta} = \frac{\partial \mathbf{I}}{\partial \beta} + \frac{\partial \mathbf{I}}{\partial X}\frac{\partial X}{\partial \beta} + \lambda_Q^T \frac{\partial R}{\partial X}\left[K\right]^{-1}\frac{\partial X_B}{\partial \beta} \tag{3.43}$$

The last term in Eq. (3.38) may be expressed as

$$\lambda_Q^T \frac{\partial R}{\partial X}\left[K\right]^{-1}\frac{\partial G}{\partial \beta} = \lambda_X^T \frac{\partial G}{\partial \beta} \tag{3.44}$$

where

$$\lambda_X = \left[K\right]^{-T}\left(\left[\frac{\partial R}{\partial X}\right]^T \lambda_Q\right) \tag{3.45}$$

is the adjoint variable for mesh sensitivity. This may be referred to as a double-adjoint method, which makes the sensitivity derivatives fully independent on the number of design variables (*ndv*). The double-adjoint formulation, however, may not significantly reduce the computational expense in the context of time-dependent problems. By introducing the adjoint variable of mesh sensitivity to Eq. (3.21), the equation now becomes

$$\frac{\mathrm{d}\mathbf{I}}{\mathrm{d}\beta} = \frac{\mathrm{d}\mathbf{I}}{\mathrm{d}\beta} + \left[\lambda_X^k\right]^T \frac{\partial X_B}{\partial \beta} + \frac{\partial \mathbf{I}}{\partial X}\frac{\partial X}{\partial \beta} \tag{3.46}$$

While this treatment leads to a formulation independent of *ndv* as well, it requires *ncyc* (number of time steps) times of linear system solutions in order to obtain the adjoint variables λ_X^k. Therefore, the double-adjoint formulation is only an improvement for time-dependent problems when *ncyc* is smaller than *ndv*.

3.5 Topology Parameterization and Sensitivity Derivatives

Topology optimization is a process of determining the locations and general shapes

of materials in a design domain. The classic homogenization-based method is utilized to conduct broadband acoustic optimization in this research. Homogenization methods are introduced in Bendsøe and Kikuchi (1988), and have become one of the standard methods in topology optimization. In topology optimization, the arbitrary dependent variable *D* is chosen to be the material properties. For example, if the design objects are acoustic materials, *D* is chosen to be the values of material density and bulk modulus

$$D = \left(\rho_e, K_e \right) \tag{3.47}$$

Given an initial discretization over the design domain, the homogenization methods usually use a uniform distribution of materials as the initial condition. That is, the design domain is considered to be a uniform material with material properties between the two or more materials for design. An interpolation scheme is required to represent the material value in each unit design cell in order to be able to use a gradient-based optimization scheme. A well-known interpolation method is the SIMP (Solid Isotropic Material with Penalisation) method (Bendsøe and Kikuchi 1988), and the formula may be written as

$$\rho_e = \rho_e^1 + \beta^t \left(\rho_e^2 - \rho_e^1 \right) \tag{3.48}$$

$$K_e = K_e^1 + \beta^t \left(K_e^2 - K_e^1 \right) \tag{3.49}$$

where $0 \le \beta \le 1$ is the design variable, and $\left(\rho_e^1, K_e^1 \right)$ and $\left(\rho_e^2, K_e^2 \right)$ represent the two types of material. A penalty factor *t* is typically used in this method to minimize the intermediate state between two materials. In order to formulate the sensitivity derivatives for topology optimization, the derivatives of the interpolation functions are needed

$$\frac{\partial \rho_e}{\partial \beta} = \left(\rho_e^2 - \rho_e^1\right) t\beta^{t-1} \tag{3.50}$$

$$\frac{\partial K_e}{\partial \beta} = \left(K_e^2 - K_e^1\right) t\beta^{t-1} \tag{3.51}$$

In the design of acoustic metamaterials, the contrasts of material properties among the multi-materials are usually large; this leads to inaccurate solutions or a large mismatch in the sensitivity derivatives. As an example, the magnitude of the sensitivity derivative is plotted in Fig. 3.9 with the SIMP method (t = 1); it can be observed that as β approaches zero, the magnitude of the sensitivity derivative increases dramatically due to the interpolation scheme. Furthermore, given a background material, the ratio of the two values (β = 0 and β = 1) scales with the material property of the chosen material for design, as shown by the black solid line in Fig. 3.10. If the chosen material has much greater values of material properties than the background material, the updates of design variables may become impossible in some cases. To circumvent this problem, a new interpolation function can be introduced to scale the functional space as

$$\rho_e = \rho_e^1 + \frac{\left(\rho_e^2 - \rho_e^1\right)^{s\beta} - 1}{\left(\rho_e^2 - \rho_e^1\right)^{s} - 1}\left(\rho_e^2 - \rho_e^1\right) \tag{3.52}$$

$$K_e = K_e^1 + \frac{\left(K_e^2 - K_e^1\right)^{s\beta} - 1}{\left(K_e^2 - K_e^1\right)^{s} - 1}\left(K_e^2 - K_e^1\right) \tag{3.53}$$

and s is the scaling factor. The corresponding derivatives are given by

$$\frac{\partial \rho_e}{\partial \beta} = \frac{s\log\left(\rho_e^2 - \rho_e^1\right)\left(\rho_e^2 - \rho_e^1\right)^{s\beta}}{\left(\rho_e^2 - \rho_e^1\right)^{s} - 1}\left(\rho_e^2 - \rho_e^1\right) \tag{3.54}$$

$$\frac{\partial K_e}{\partial \beta} = \frac{s \log\left(K_e^2 - K_e^1\right)\left(K_e^2 - K_e^1\right)^{s\beta}}{\left(K_e^2 - K_e^1\right)^s - 1}\left(K_e^2 - K_e^1\right) \tag{3.55}$$

When an appropriate value of the scaling factor s is chosen, the sensitivity derivatives can be changed to a similar order of magnitude. This is favorable in optimization algorithms since the searching of the optimal point would be less dependent upon the material property differences. As an example, the ratio of the derivatives in Eqs. (3.49-3.50) can be manipulated (with s = 1.25), such that it is approximately the inverse of the ratio of the sensitivity derivatives based on linear interpolations, as shown by the red dashed line in Fig. 3.10. As a result, the ratio of sensitivity derivatives is adjusted to be close to 1, as shown by blue dashed-dot line in Fig. 3.10. Because of its nature, this scheme may be called the Scaled Material Interpolation (SMI). Further investigation is needed to make the scaling more independent of the choices of *s*.

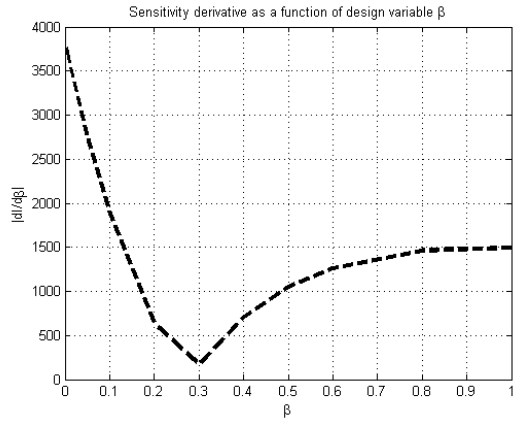

Figure 3.9 Sensitivity derivative as a function of design variable β. $\rho_e^1 = K_e^1 = 1$ and $\rho_e^2 = K_e^2 = 3$.

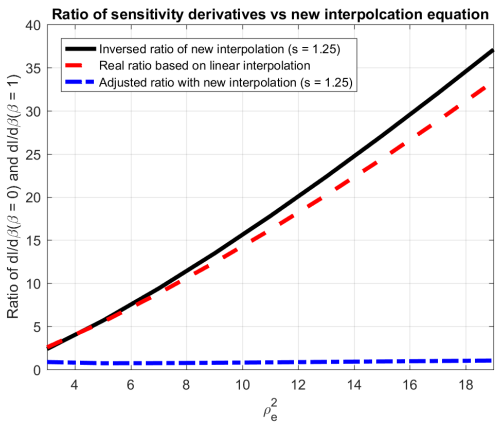

Figure 3.10 Ratio of sensitivity derivatives and SMI function values as ρ_e^2 and K_e^2 change. Scaling factor s = 1.25

While the function of the penalty power, p, in both interpolation functions is not directly related to the cost function, another factor, q, can be introduced to alter the cost function such that the intermediate state can be effectively avoided

$$\mathbf{I}^* = \alpha_q \mathbf{I} \tag{3.56}$$

where

$$\alpha_q = 1 + q\sum_{i=1}^{ndv}\left(\beta_i - 0.5\right)^2 \tag{3.57}$$

is the penalty factor to the cost function. Note that the cost function **I*** in Eq. (3.56) becomes larger than the original cost function **I** if some design variables β_i are in between 0 and 1, and it returns to the original value at their upper or lower bounds.

To seek the optimal shape for a given cost function, the computational domain usually requires a highly refined mesh in order to obtain a well-defined geometry. This procedure, however, would dramatically increase the computational overhead and make

the simulation prohibitively expensive since time step is limited on a fine computational mesh. Alternatively, shape optimization can be subsequently used on the design produced from topology optimization. In this case, the topology optimization may be performed on a relatively coarse mesh, and the resulting procedure referred to as sequential topology and shape optimization.

CHAPTER 4

RESULTS AND DISCUSSION

4.1 Simulation Results

The proposed acoustics solver with the stabilized finite element formulation is first examined on a case with two layered materials. In the test case, an acoustic wave is initiated from the left end of material 1 with $\rho_e = 1$ and $K_e = 1$, it then hits the material interface and is partially reflected and partially transmitted. Material 2 has properties of $\rho_e = 4$ and $K_e = 1$. If the incident pressure pulse has magnitude p_0, then the transmitted pulse has magnitude $C_T p_0$ and the reflected pulse has magnitude $C_R p_0$, where the transmission and reflection coefficients are given by

$$C_T = \frac{2Z^2}{Z^1 + Z^2},\ C_R = \frac{Z^2 - Z^1}{Z^1 + Z^2} \tag{4.1}$$

and Z is the impedance. In this example, $C_T = 4/3$ and $C_R = 1/3$.

A grid convergence study is conducted, which indicates by Fig. 4.1 that the solutions with linear elements leads to second order accuracy (slope = 2.09). Third order accuracy (slope = 3.15) is obtained with quadratic elements.

The two dimensional elastic wave solver is tested in an elastic solid with a stiff inclusion (LeVeque 2002) with quadratic elements. As shown in Fig. 4.2, in this case, the elastic wave is propagating into a solid that has embedded within it an inclusion made out

of a stiffer material with λ = 200 and μ = 100. The background material has material properties of λ = 2 and μ = 1. The density is the same everywhere, ρ = 1. The wave is initiated by setting the initial condition as the eigenvector corresponding to eigenvalue c_p of the matrix of the left side of Eq. (2.33)

$$Q^0 = \exp\left(-\frac{1}{2}\frac{\left(x - x_0\right)^2}{\sigma^2} \right) \begin{bmatrix} \lambda + 2\mu n_x^2 \\ \lambda + 2\mu n_y^2 \\ 2\mu n_x n_y \\ -n_x c_p \\ -n_y c_p \end{bmatrix} \tag{4.2}$$

with $\hat{n} = \begin{bmatrix} 1 & 0 \end{bmatrix}^T$, σ = 0.01 and x_0 = 0.2. As shown in Fig. 4.3, a compression wave is created, followed by a mixed P- and S- waves due to its interactions with the free boundaries and the inclusion. Besides, the distortion of the stiff inclusion is much smaller than the background material. Elastic waves are rapidly bouncing back and forth in the stiff inclusion along with its motion.

Figure 4.4 shows a case of acoustic wave propagating in three dimensions. The solution field is perturbed by setting an initial condition as

$$Q^0 = \begin{cases} \begin{bmatrix} 1 & 0 & 0 & 0 \end{bmatrix}^T, r \le 1 \\ \begin{bmatrix} 0 & 0 & 0 & 0 \end{bmatrix}^T, r > 1 \end{cases} \tag{4.3}$$

with $r = (x + 1.5)^2 + y^2 + z^2$. As time evolves, the acoustic wave, initiated by a pulse in the -x direction of the sphere, propagates away from the center of the pulse and is scattered by the sphere. The material properties of the sphere are ρ_e = 4 and K_e = 100 relative to the background air. The instantaneous pressure fields on a sphere and the X-plane are plotted, and the record of solution in nondimensional units at a sensor in the +x direction away from the sphere at (1.5, 0, 0) is shown in Fig. 4.5.

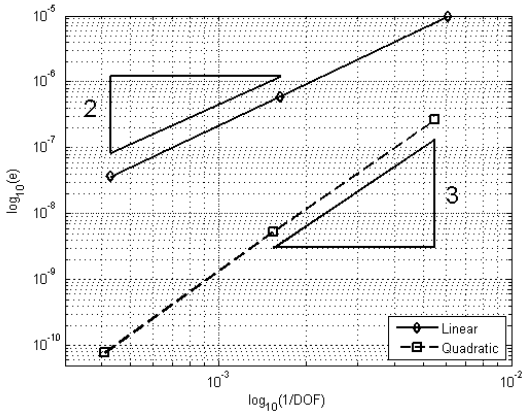

Figure 4.1 Orders of accuracy of the SUPG solver with linear and quadratic elements.

Figure 4.2 An elastic solid with stiff inclusion.

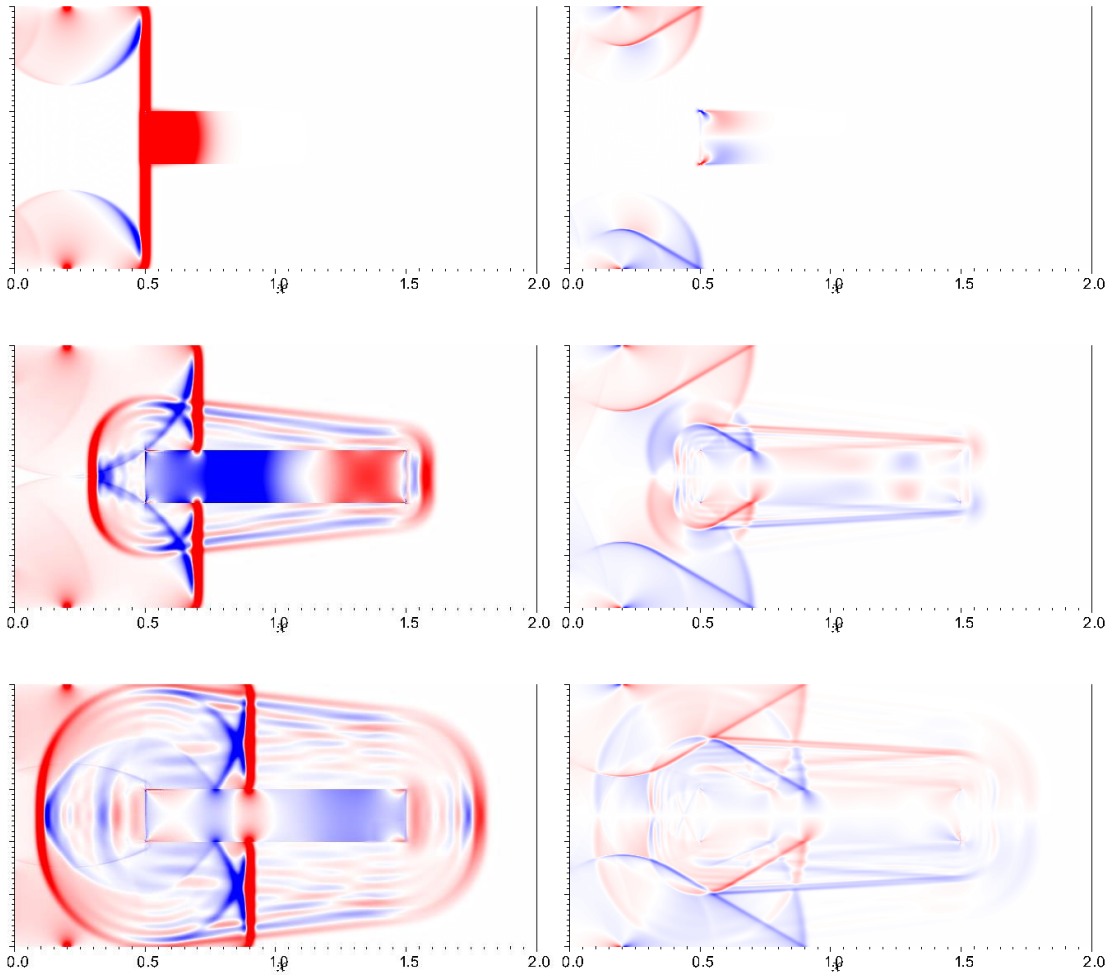

Figure 4.3 Elastic wave propagation in an elastic solid with stiff inclusion at t = 0.3, 0.5 and 0.7. Left shows $\sigma_{xx} + \sigma_{yy}$, and right shows σ_{xy}.

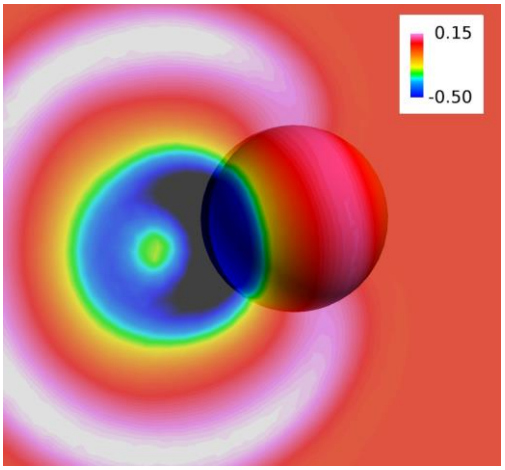

Figure 4.4 An instantaneous pressure field of a pulse hitting a sphere.

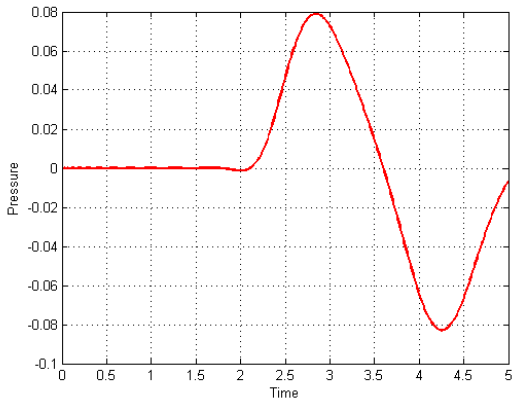

Figure 4.5 The time-domain solution of pressure at a sensor behind the sphere.

4.2 Verification and Timing of the Optimization Framework

Although the finite difference method for sensitivity derivatives is not practical due to its cancellation errors and expenses associated with the number of design variables, it serves as an appropriate technique to verify the forward and adjoint based sensitivity calculations. Figure 4.6 shows the sensitivity derivatives obtained using the finite difference, forward formulation, and adjoint formulation, and the differences are

negligible. In terms of computational time, the three methods show different behaviors. As shown in Fig. 4.7, the computational time of the adjoint based calculation remains almost constant as the number of design variables grows. In contrast, both the finite difference method and the forward sensitivity calculation show a linear growth in computational time. It is also interesting to notice that, when the number of design variables is smaller than 3, finite difference method takes the shortest time to obtain the sensitivity derivatives, and the adjoint based calculation, due to the file I/O and the required complex linear matrix system solver, is slowest in this case.

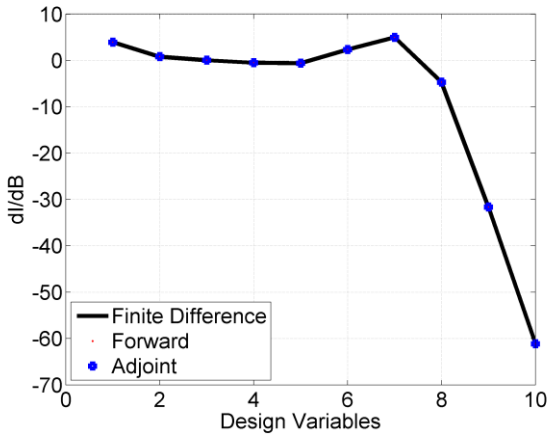

Figure 4.6 Verification of the sensitivity derivatives with the finite difference method

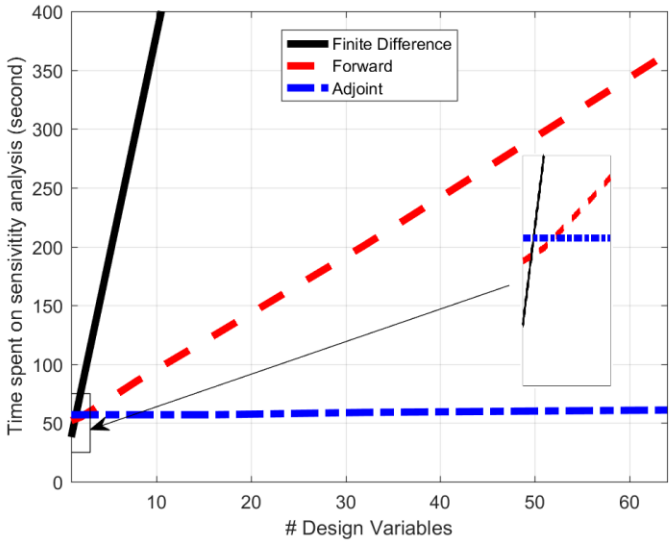

Figure 4.7 Computational times in terms of the number of design variables by the finite difference method, forward and adjoint based sensitivity calculation

Before the proposed shape and topology optimization framework can be applied to practical designs, it is important to verify it with an inverse design process. That is, the gradient-based optimization should be capable of recovering a known design, given an arbitrary initial configuration.

The verification case is chosen to be the inverse design of a unit cell with a known frequency-domain solution $\hat{p}^0$,

$$\begin{aligned} &\min \mathbf{I} = \int_{\omega_1}^{\omega_2} \int_{\Gamma} \left(\hat{p} - \hat{p}^0 \right)^2 d\Gamma d\omega \\ &\text{s.t. } R^k = 0,\ k = 1,\ldots,ncyc \\ &\beta_{\mathrm{L}} \le \beta \le \beta_{\mathrm{U}} \end{aligned} \tag{4.4}$$

The topology optimization is initialized with an arbitrary distribution of the material density, and the cost function to be minimized is chosen to be the L_2-norm of the

differences between the current and the original frequency-domain solution with no penalty. The values of the design variables β are between 0 (β_L) and 1 (β_U).

As expected, the distribution of material converges back to the original shape as shown in Fig. 4.8f. Note that due to the fact that the sensor locations are not adjacent to the target shape, the final shape in Fig. 4.8e is only an approximation to the original.

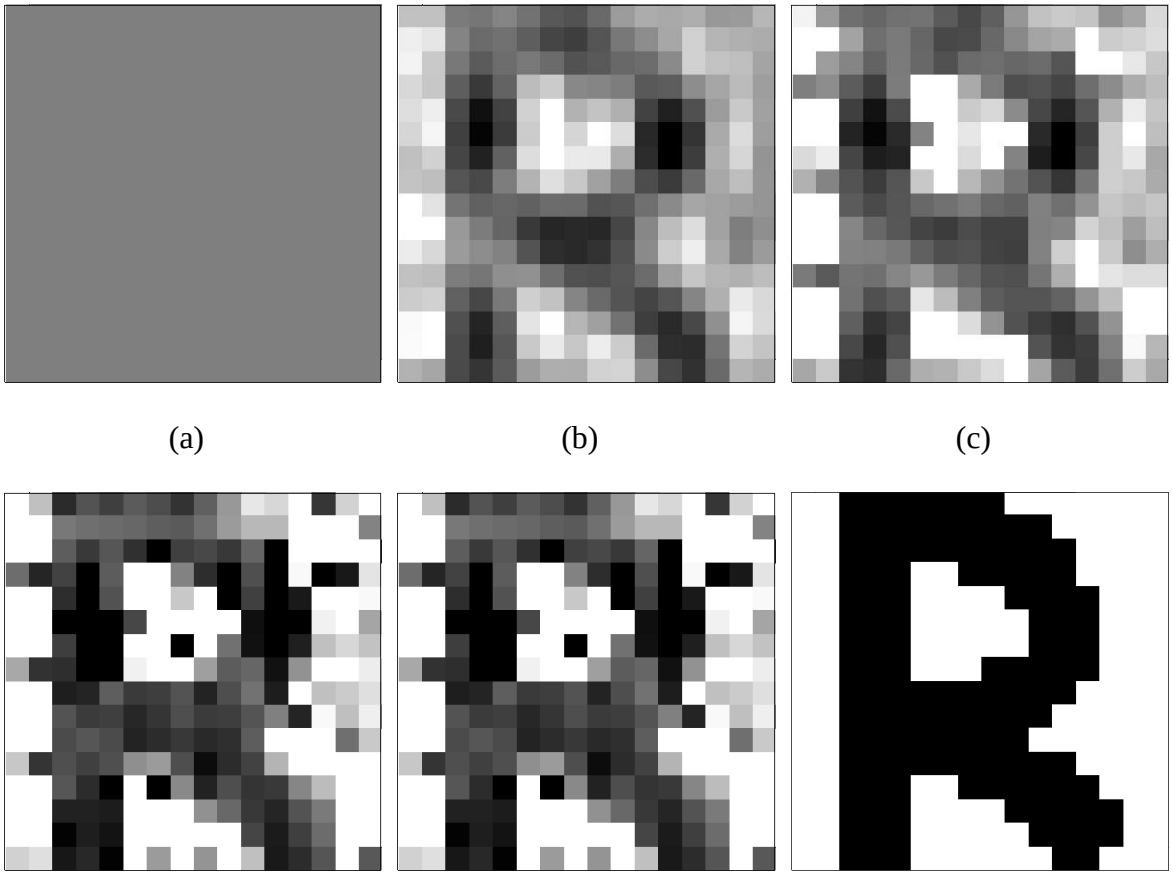

(a) (b) (c)

(d) (e) (f)

Figure 4.8 Shape recovery in an inverse optimization with a given frequency domain solution. (a-e) The shape evolution during the inverse design iterations. (f) The target shape.

4.3 Design of Broadband Acoustic Cloaking

An acoustic cloak is a hypothetical device used to conceal an object from detecting waves. Such cloaking can be applicable to stealth aircraft using absorbing materials to minimize the wave emissions. Theoretical cloaking based on coordinate transformation methods have been proposed in several studies (Pendry, Schurig, and Smith 2006; Cummer et al. 2006). This principle can be approximated by multilayered structures with isotropic materials (Chen and Chan 2007). However, the efficiency of using conventional simple isotropic media to design cloaking devices remains questionable.

Recently the use of negative refraction metamaterials for the design of cloaking has become an active area of research (Zhang, Xia, and Fang 2011). These metamaterials are engineered materials that have acoustic properties that cannot easily be found in nature. Such properties include negative effective bulk modulus and mass density, and can be applied for soundproofing, acoustic cloaking, seismic shields, etc. Metamaterials are dedicated to sub-wavelength structures, and a careful manipulation of these structures greatly affects the overall behaviors of the material. However, metamaterials typically involve complex micro-structured inclusions, which make manufacturing difficult.

Acoustic cloaking can be alternatively designed using topology optimization. Since the goal is to minimize the scattering pressure field, the design can be formulated as a classical optimization problem with properly defined cost functions. Similar work has been previously performed on topologically optimized cloaking, but these studies have been limited to certain frequency points (García-Chocano et al. 2011; Andkjær and Sigmund 2013).

In this section, gradient-based topology optimization is applied to acoustic cloaking

(Lin, Newman III, and Anderson 2016). The optimization problem for acoustic cloaking may be formulated as

$$\begin{aligned} &\min \mathbf{I} = \int_{\omega_1}^{\omega_2} \int_{\Gamma} \left(\hat{p} - \hat{p}^0 \right)^2 d\Gamma d\omega \\ &\text{s.t. } R^k = 0,\ k = 1,...,ncyc \\ &\beta_L \le \beta \le \beta_U \end{aligned} \tag{4.5}$$

where $\hat{p}$ is the Fourier transformation of the time domain solution p, and $\hat{p}^*$ is the reference solution. In the case of acoustic cloaking, the reference solution is chosen to be the incident wave solution.

With a cylinder as the object of interest, the computations are performed by simulating a Gaussian pulse propagating in the normal incident direction (+x direction). The radius of the cylinder is 7 cm, and the center frequency of the Gaussian pulse is 2 kHz. In this research, the material properties of the inclusion are $\rho_e^2 = 4\rho_e^1$ and $K_e^2 = 4K_e^1$, where the index 1 indicates the inclusion and 2 indicates the background material. First order absorbing boundary conditions are applied to the outer boundaries.

Figures 4.9-4.11 show the incident and total pressure contours at three frequencies corresponding to 1.9, 2.0 and 2.1 kHz, respectively. As seen, the incident waves are scattered to different degrees for these frequencies. Note, in order to highlight the near-body and far-field wave behaviors, the wave propagation inside the inclusion is not shown.

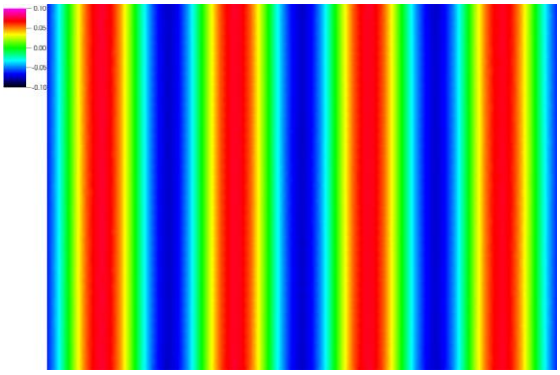

(a) Incident pressure wave

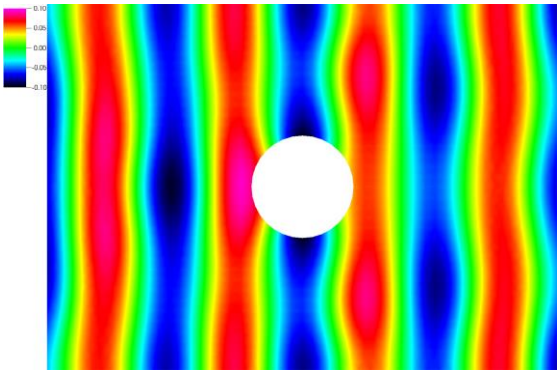

(b) Total pressure wave

Figure 4.9 Incident and total pressure contours at 1.9 kHz

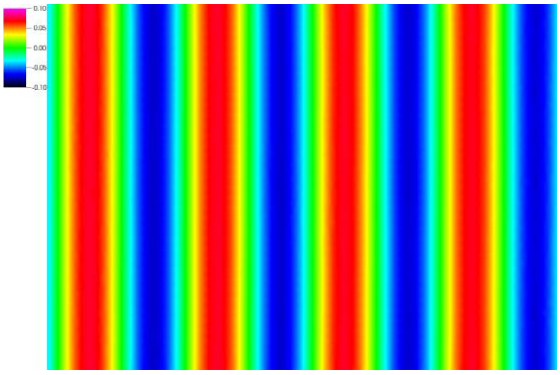

(a) Incident pressure wave

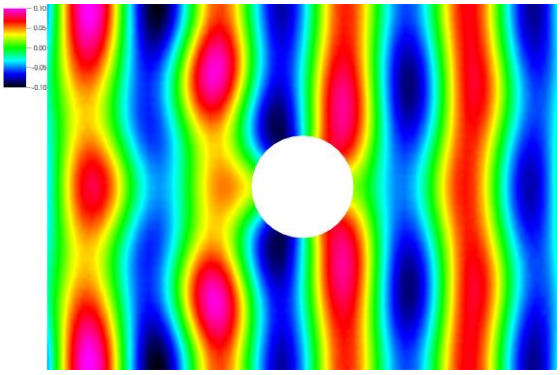

(b) Total pressure wave

Figure 4.10 Incident and total pressure contours at 2.0 kHz

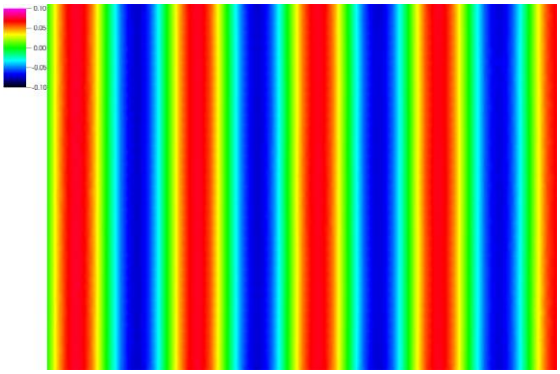

(a) Incident pressure wave

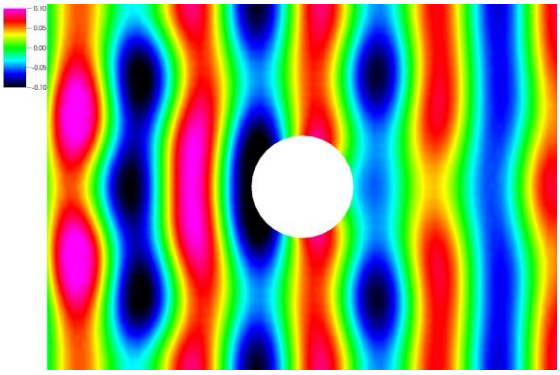

(b) Total pressure wave

Figure 4.11 Incident and total pressure contours at 2.1 kHz

Topology optimization is conducted to design the shapes in the vicinity of the inclusion in order to match the reflected and transmitted waves with the incident wave profiles. The configuration of the optimization can be illustrated by Fig. 4.12, where a randomly generated geometry is shown. The design domain is specified to be 50 cm by 50 cm centered at the cylinder. The design domain is constrained to have symmetries in the *x* and *y* directions. During the optimization, each dark square in Fig. 4.12 can be considered in the design space.

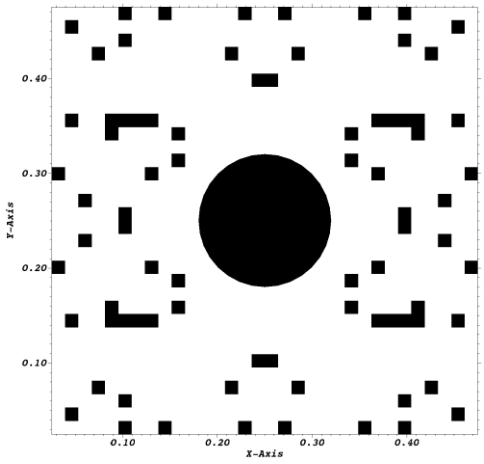

Figure 4.12 Sample illustration of the topology optimization with randomly generated geometries near the inclusion

In order to examine the efficiency of acoustic cloaking at different frequency levels, two optimization cases are studied. The first optimization case is chosen with the target of minimizing the cost function specified in Eq. (4.4) for a narrowband. That is, one frequency point $\omega_1 = \omega_2 = 2$ kHz is specified for the cost function **I** as in Eq. (4.5). In the second optimization case, the frequency range is extended from $\omega_1 = 1.9$ kHz to $\omega_2 = 2.1$ kHz and will be referred to as broadband. In both cases, the cost function is integrated on the transmission lines Γ_T (transmission) and Γ_R (reflection). Starting with uniform distribution of the material ($\beta = 0.5$), the optimized geometries are shown in Figs. 4.13 and 4.14 for the narrowband and broadband designs, respectively. Note that since the design variables vary continuously over the domain, the final geometries may be determined using a penalty factor to minimize intermediate material states or the topology optimization may be followed by a shape optimization as described in Lin et al (2016b).

Once again, corresponding to frequency points 1.9, 2.0 and 2.1 kHz, the total pressure contours of the two optimization cases are shown in Figs. 4.15-4.17 As can be observed, the optimized cloaking for narrowband works efficiently at its target frequency (2.0 kHz) since the reflected and transmitted waves are recovered from scattering (Fig. 4.16a). This design, however, is not suitable at different frequency points, such as 1.9 kHz (Fig. 4.15a) and 2.1 kHz (Fig. 4.17a). In comparison, the optimized cloaking for broadband improves performance over the range of frequencies considered (Figs. 4.15b, 4.16b and 4.17b). It should be noted, that in the broadband optimization, although the pressure distributions upstream and downstream of the design domain are visually similar to the incident pressure distribution at all three frequency points, the actual performance of the cloaking is not necessarily optimal. Quantifying the acoustic cloaking performance using the cost function specified in Eq. (4.4), it is realized that the narrowband optimization leads to superior cloaking performance at its target frequency 2.0 kHz (Fig. 4.18). However, the cost function values for the broadband optimization are lower over the frequency range considered.

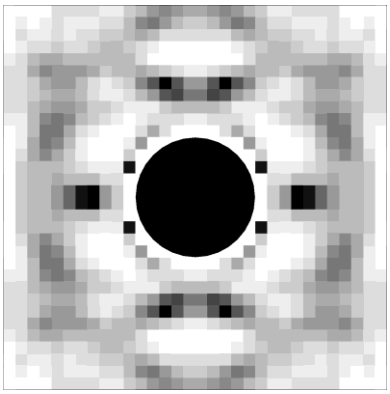

Figure 4.13 The optimized cloaking for the narrowband case

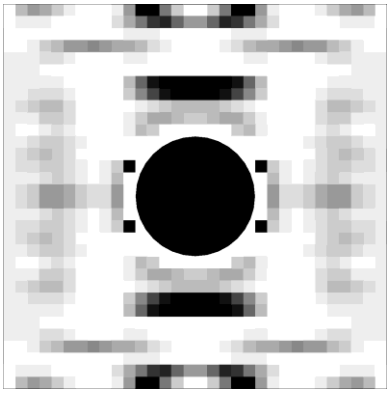

Figure 4.14 The optimized cloaking for the broadband case

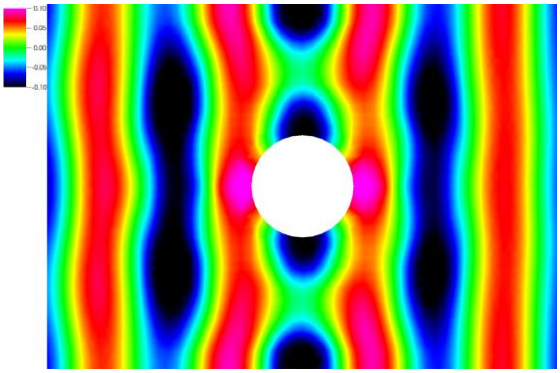

(a) Narrowband optimization

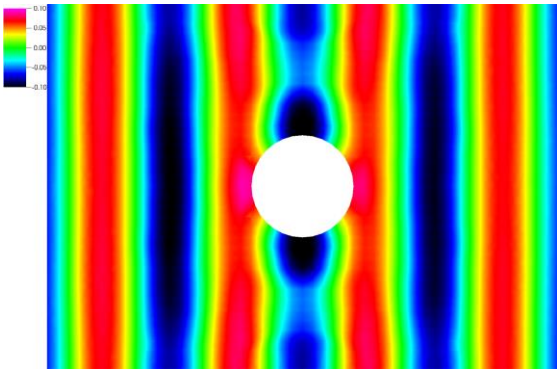

(b) Broadband optimization

Figure 4.15 Total pressure contours at 1.9 kHz with cloaking

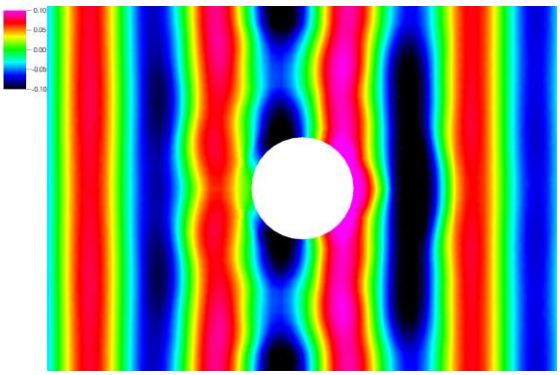

(a) Narrowband optimization

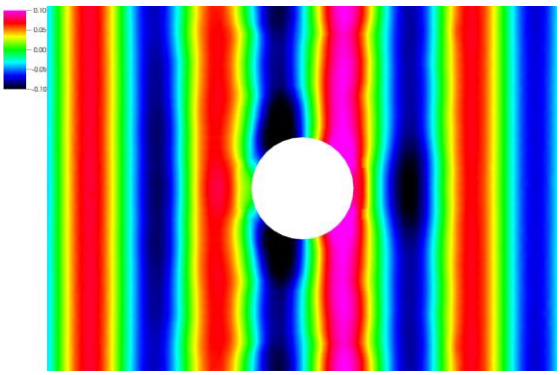

(b) Broadband optimization

Figure 4.16 Total pressure contours at 2.0 kHz with cloaking

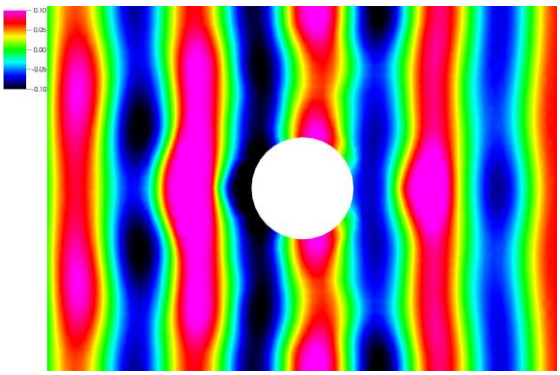

(a) Narrowband optimization

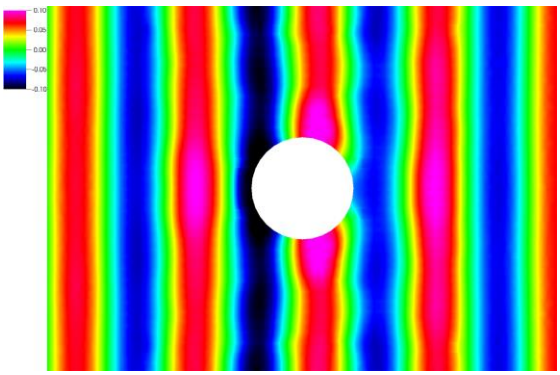

(b) Broadband optimization

Figure 4.17 Total pressure contours at 2.1 kHz with cloaking

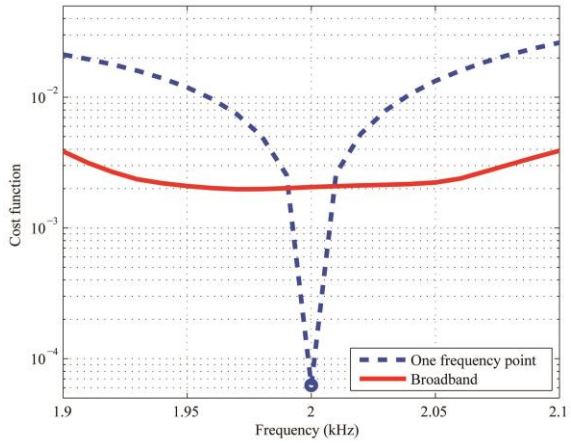

Figure 4.18 The cost function values of the narrowband (blue dashed line) and broadband (red solid line) optimizations. Smaller values indicate better performance

4.3 Optimization of Acoustic Metamaterials

A periodic square structure of sub-wavelength scale is considered as the baseline case for acoustic metamaterials in air. The unit cell is a square with edge length a = 1 cm. The frequency range of interest is from 0.5 kHz to 3 kHz, corresponding to wavelengths ranging from approximately 12 to 69 unit lengths. The inclusion is chosen to be steel with material properties as $\rho_e^2 = 6131\rho_e^1$ and $K_e^2 = 8\times10^5 K_e^1$.

The simulation is initiated wtih a Gaussian pulse in the +x direction, and sensors are used to collect transmissions and reflections along the x-axis. In addition, periodic boundary conditions are applied to the upper and lower parts of the domain, and absorbing boundary conditions (Mur 1981) are applied to the left and right ends. The design domain is enforced to have symmetries in the x and y directions. The transmission and reflection coefficients are calculated by transforming the time-domain to frequency

domain, which are in turn used to retrieve the effective refractive index n and acoustic impedance Z (Fokin et al. 2007)

$$n = \frac{\cos^{-1}\left(\frac{1-R^2+T^2}{2T}\right)}{kd} \tag{4.6}$$

$$Z^2 = \frac{(1+R)^2 - T^2}{(1-R)^2 - T^2} \tag{4.7}$$

where k is the wave number, and d is the effective slab thickness. In order to use the effective material properties in optimization, the partial derivatives of n and Z with respect to the solution Q^k need to be derived in both forward and adjoint formulations as given in Eqs. (3.14) and (3.20).

An optimization procedure is conducted to achieve the desired material properties. The first optimization performs an inverse design of the refractive index and impedance as

$$\begin{aligned} &\min \mathbf{I} = \alpha_q \int_{\omega_1}^{\omega_2} \left[\left(Z - Z^*\right)^2 + \left(n - n^*\right)^2 \right] d\omega \\ &\text{s.t. } R^k = 0,\ k = 1,...,ncyc \\ &\beta_L \le \beta \le \beta_U \end{aligned} \tag{4.8}$$

where Z^* = 2.0, n^* = 2.0. The topology optimization is conducted on a 32×32 computational mesh. It is observed that without penalty (q = 0) the optimal design is achieved with many intermediate densities (gray area). This in turn makes the determination of the geometry very difficult, as seen in Fig. 4.19a. In comparison, the optimal geometry is less ambiguous as the penalty factor q is increased. Figure 4.19b shows the optimal design with q = 1, where the gray area is greatly reduced, and

intermittency disappears when q is increased to 10 and 100, as seen in Figs. 4.19c and 4.19d. Thus increasing the penalty factor q results in minimized intermediate states between two materials. However, the resulting geometries are found to be different from each other due to the change of the cost functions.

As a comparison to the penalty-based homogenization method, the sequential topology and shape optimization is applied to the design of an acoustic metamaterial. The topology optimization is conducted with $q = 0$ on a 10×10 design domain as shown in Fig. 4.20a, and the resulting geometry is employed to construct the initial geometry for the shape optimization as illustrated in Fig. 4.20b. The construction of the shape is based on the real solid boundary and the centroids of the intermediate states (gray areas). Therefore, the geometry is only approximated based on the topology optimization. The final optimized shape is shown in Fig. 4.20c, and the effective material properties are given in Fig. 4.21.

The cost function values of the cases with penalty methods are illustrated in Fig. 4.22, which correspond to the geometries in Figs. 4.19b, 4.19c, 4.19d and 4.20c, respectively. It indicates that, in the current design, the sequential method has advantages over the penalty-based method in that it leads to a smooth and unambiguous geometry and results in the best design performance. However, since the choice of penalty factor appears to greatly affect the optimization results, a more detailed investigation is recommended for the future work.

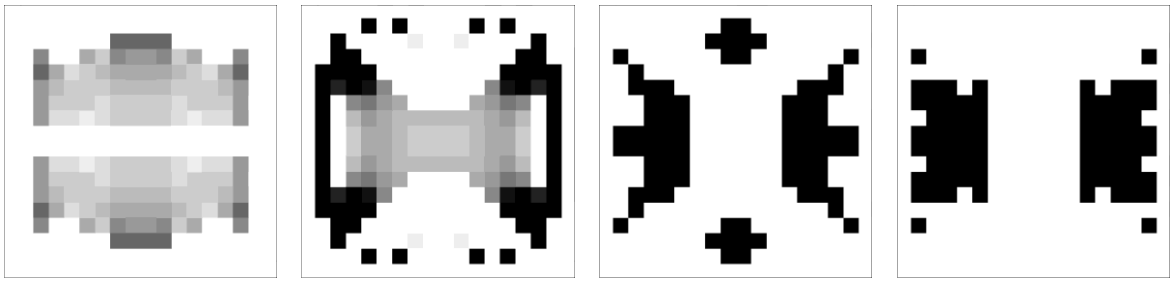

(a) (b) (c) (d)

Figure 4.19. Topology optimizations on a 32×32 mesh. (a) No penalty, (b) q = 1, (c) q = 10, (d) q = 100.

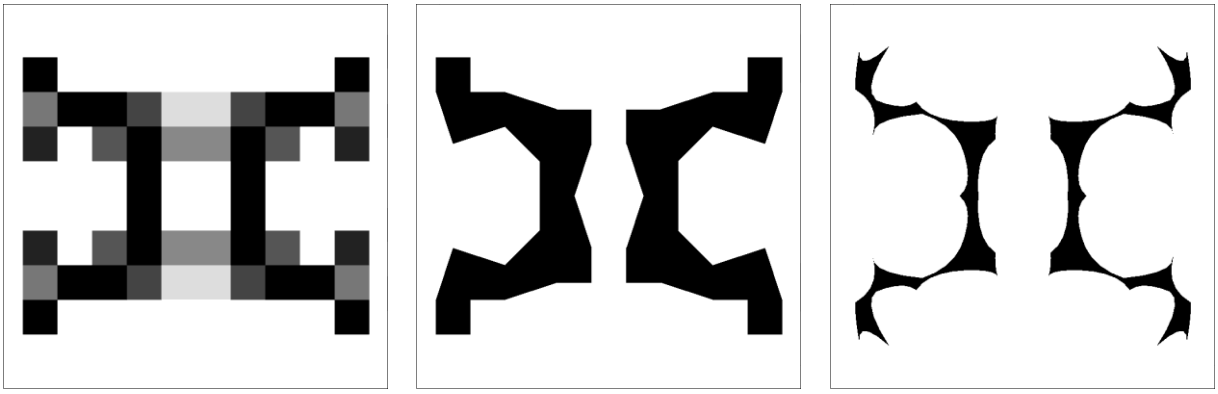

(a) (b) (c)

Figure 4.20 Topology optimization followed by a shape optimization. (a) Topology optimization without penalty on a 10×10 mesh, (b) arbitrary shape representation of the topologically optimized geometry, (c) optimized shape.

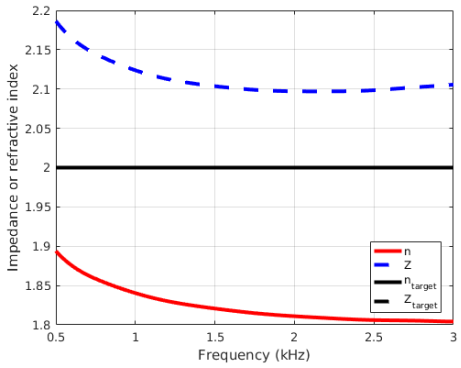

Figure 4.21 Effective impedance and refractive indices of the optimized shape. Red and blue lines represent the effective material properties and black lines represent the targets.

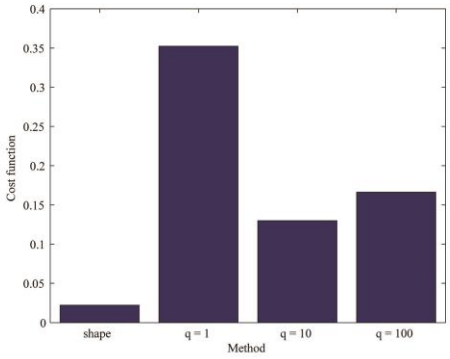

Figure 4.22 Comparison of the final cost function values by the sequential method and homogenization method with penalties.

A shape optimization procedure is also conducted on a three dimensional slab to achieve the desired material properties (Lin, Newman, et al. 2016b). The optimization seeks to maximize the refractive index while minimizing impedance with ω_1 = 0.5 kHz and ω_2 = 2 kHz, which corresponds to the wavelengths approximately equal to 9 and 69

unit cell sizes. The target values are $Z^* = 1.0$ and $n^* = 0.91$. An optimal shape is achieved after several design iterations, and the surface deformation is shown in Figs. 4.23a and 4.23b. It is observed in Figs. 4.24 and 4.25 that with the optimal shape, the values of both effective refractive index and impedance are closer to the desired values than the original flat slab.

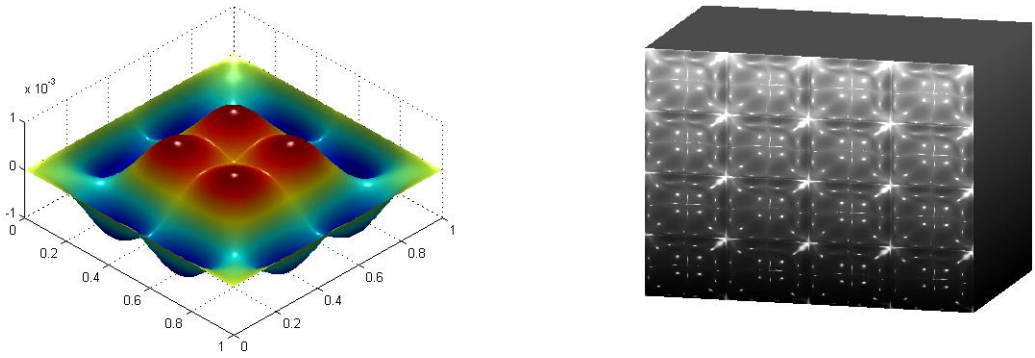

(a) (b)

Figure 4.23. (a) Optimized surface of the metamaterial, and (b) a view of the surface of the metamaterial to achieve desired effective material properties.

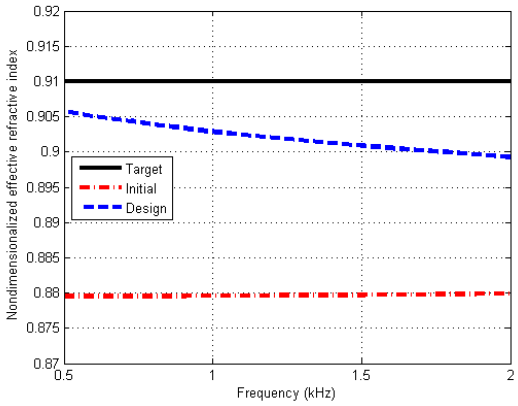

Figure 4.24 The initial, target and final effective refractive index of the metamaterial.

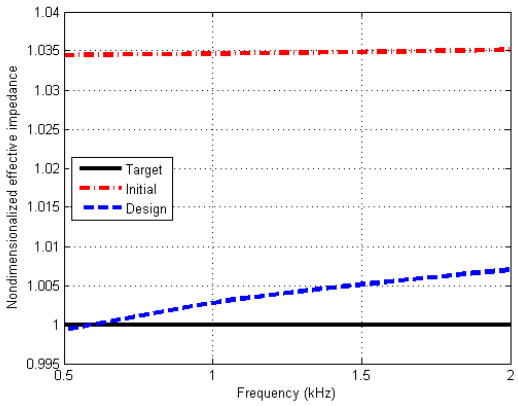

Figure 4.25 The initial, target and final effective impedance of the metamaterial.

4.4 Optimization of Phononic Crystals

The analysis of the response of composite materials typically starts by calculating the band-structures of a unit cell. Based on the Floquet-Bloch wave theory mentioned in Chapter 2, the solutions to the periodic eigen-problems are eigenvalues $\omega(k)$ as continuous functions of Bloch wave vector k, forming discrete bands. Furthermore, due to the symmetry of the unit cell in phononic crystals, the band-diagram can be plotted by restricting the wave vectors to the first Brillouin zone.

In practice, the response of a structure to the external source of excitation may be calculated. In this section, the application of the acoustic wave solver on a single square lattice is considered. The computations are performed by simulating a Gaussian pulse propagating in the normal incident direction (+x direction) to the square lattices, or along the ΓX plane in the sense of the first Brillouin zone (Brillouin 2003). The unit cell is a square with edge length a = 50 cm. The frequency range of interest is from 0.5 kHz to 3 kHz, corresponding to wavelengths ranging from approximately 1 to 7 unit lengths.

The attenuation of the sound pressure at the sensors, in a frequency range, is selected to be the design target

$$\begin{aligned} &\min \mathbf{I} = \alpha_q \int_{\omega_1}^{\omega_2} \hat{p}\,\overline{\hat{p}}\, d\omega \\ &\text{s.t. } R^k = 0,\ k = 1,...,ncyc \\ &\beta_L \le \beta \le \beta_U \end{aligned} \tag{4.9}$$

where ω_1 = 0.5 kHz and ω_2 = 3 kHz, and $\hat{p}$ is the Fourier transforms of pressures recorded at the sensor with the periodic structures. Note that in this optimization configuration, because of the symmetric properties of the structure, the design variables are only applied to a quadrant and the deformations are mirrored in the x and y directions. The optimization is conducted for 3 cases. In case 1, the material properties of the inclusion are $\rho_e^2 = 2\rho_e^1$ and $K_e^2 = 2K_e^1$, in case 2 $\rho_e^2 = 4\rho_e^1$ and $K_e^2 = 4K_e^1$, and in case 3 are $\rho_e^2 = 8\rho_e^1$ and $K_e^2 = 8K_e^1$.

Since it is observed that without penalty (q = 0) the optimal design does not usually results in a well-defined geometry, the results obtained by setting appropriate penalty factors are shown in Figs. 4.26-4.28, which correspond to cases 1 to 3 respectively. Figures 4.26a, 4.26b and 4.26c show the optimal designs on coarse, medium and fine meshes respectively. As the mesh is refined, the geometry is better resolved. Based on topologically optimized geometry with no penalty on a coarse mesh, the final geometry obtained by the sequential topology and shape optimization is given in Fig. 8d. This optimized shape, however, differs from the topology optimization results on the finer meshes. Similar trends are observed in Figs. 4.27 and 4.28.

In order to quantify the performance for each design, the final cost function values

are shown in Fig. 4.29. It may be observed that the minimizations of the cost function values are not consistent in the three cases. The sequential topology and shape optimization leads to the minimum cost function in case 2, but this is not the simulation for cases 2 and 3. In all cases the cost function values are of the same orders of magnitude. Nevertheless, due to the fact that the sequential method uses much less computational resources (i.e., smaller design space, less computational overhead), it can still be distinguished as the most effective method in the current research.

The transmission coefficients of each case with the sequential method are shown in Figs. 4.30-4.32, with the normalized pressure contours corresponding to 1.1 kHz, 1.75 kHz and 2.4 kHz. The pressure contours illustrate that the transmissions are greatly reduced at the frequency points where the corresponding transmission coefficients are low. At a frequency point where the coefficient is relatively high, sound pressure is still detectable (Fig. 4.30c).

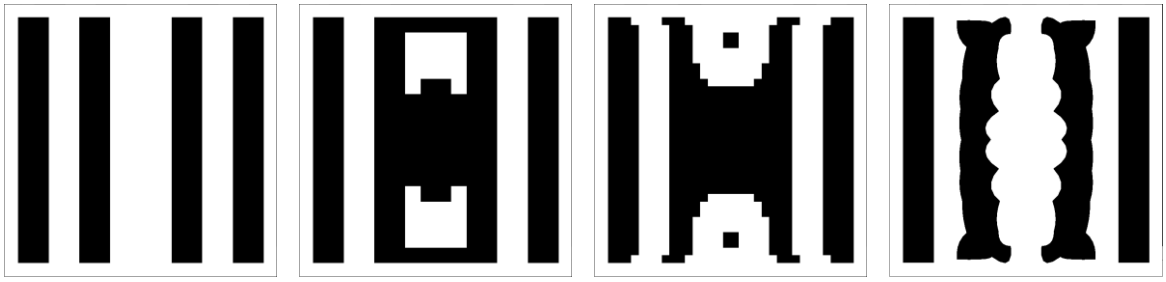

(a) (b) (c) (d)

Figure 4.26 Minimization of acoustic transmission in the case 1 with $\rho_e^2 = 2\rho_e^1$ and $K_e^2 = 2K_e^1$. Topology optimization on a (a) coarse mesh, (b) medium mesh, (c) fine mesh, (d) sequential topology and shape optimizations

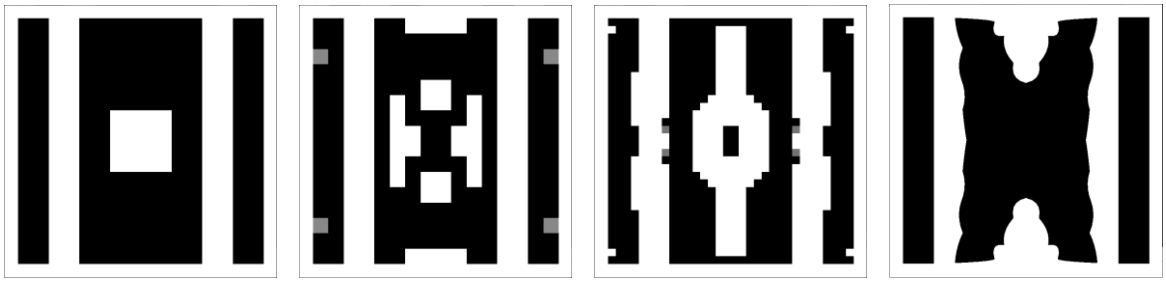

(a) (b) (c) (d)

Figure 4.27 Minimization of acoustic transmission in the case 2 with $\rho_e^2 = 4\rho_e^1$ and $K_e^2 = 4K_e^1$. Topology optimization on a (a) coarse mesh, (b) medium mesh, (c) fine mesh, (d) sequential topology and shape optimizations

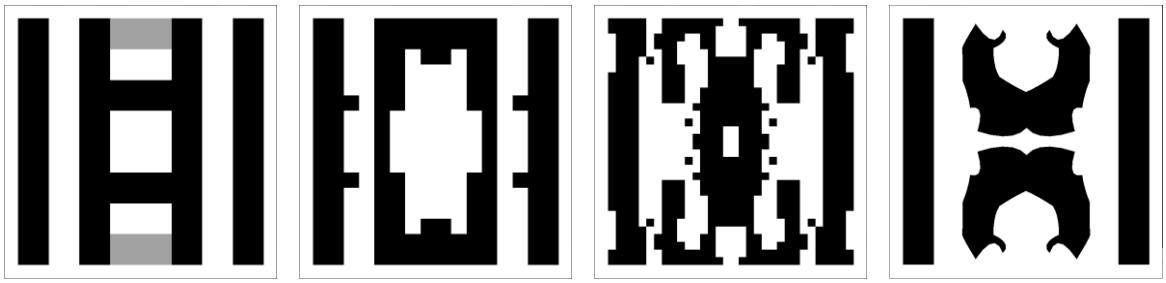

(a) (b) (c) (d)

Figure 4.28 Minimization of acoustic transmission in the case 3 with $\rho_e^2 = 8\rho_e^1$ and $K_e^2 = 8K_e^1$. Topology optimization on a (a) coarse mesh, (b) medium mesh, (c) fine mesh, (d) sequential topology and shape optimizations

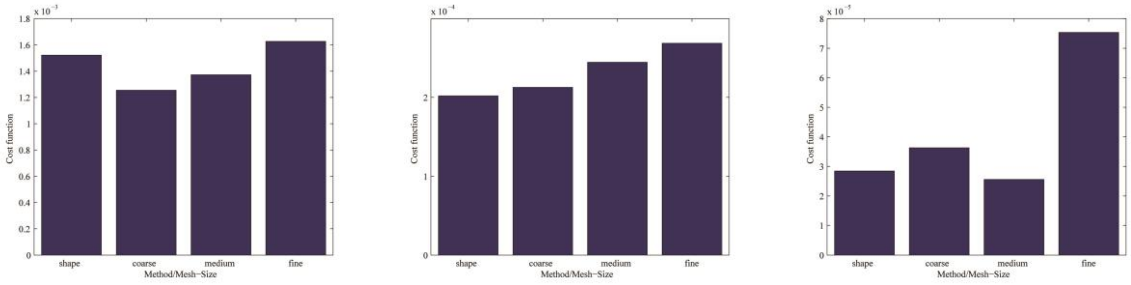

(a) (b) (c)

Figure 4.29 Comparison of the final cost function values by the sequential method and homogenization method on different meshes. (a) Case 1 with $\rho_e^2 = 2\rho_e^1$ and $K_e^2 = 2K_e^1$. (b) Case 2 with $\rho_e^2 = 4\rho_e^1$ and $K_e^2 = 4K_e^1$. (c) Case 3 with $\rho_e^2 = 8\rho_e^1$ and $K_e^2 = 8K_e^1$.

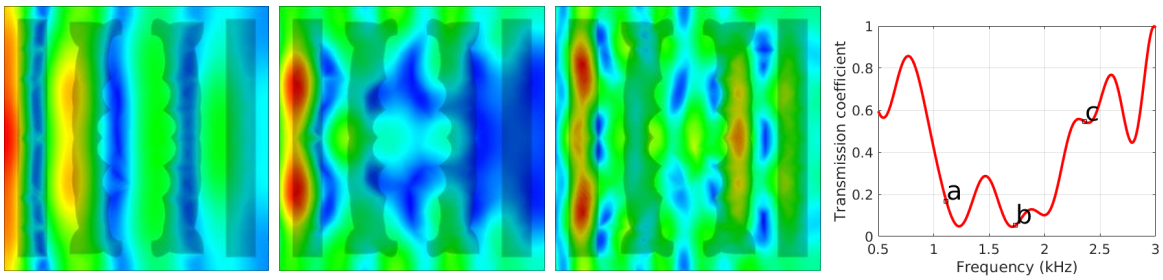

(a) (b) (c) (d)

Figure 4.30 Optimization results of case 1 with $\rho_e^2 = 2\rho_e^1$ and $K_e^2 = 2K_e^1$. Normalized pressure contours (blue-red: low-high) at (a) 1.1 kHz, (b) 1.75 kHz, (c) 2.4 kHz. (d) Transmission coefficient.

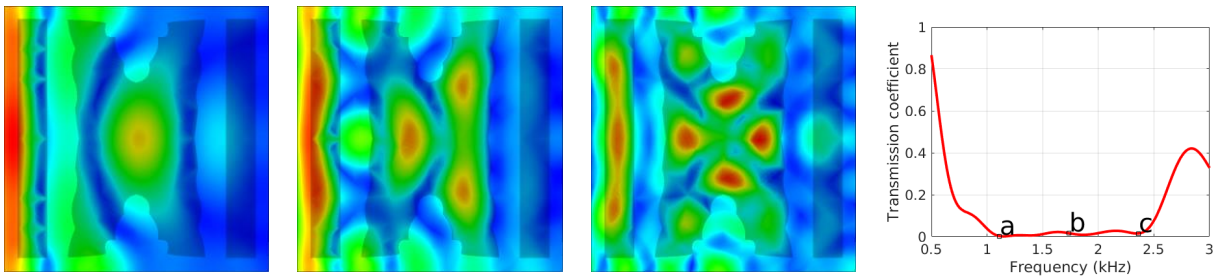

(a) (b) (c) (d)

Figure 4.31 Optimization results of case 2 with $\rho_e^2 = 4\rho_e^1$ and $K_e^2 = 4K_e^1$. Normalized pressure contours (blue-red: low-high) at (a) 1.1 kHz, (b) 1.75 kHz, (c) 2.4 kHz. (d) Transmission coefficient.

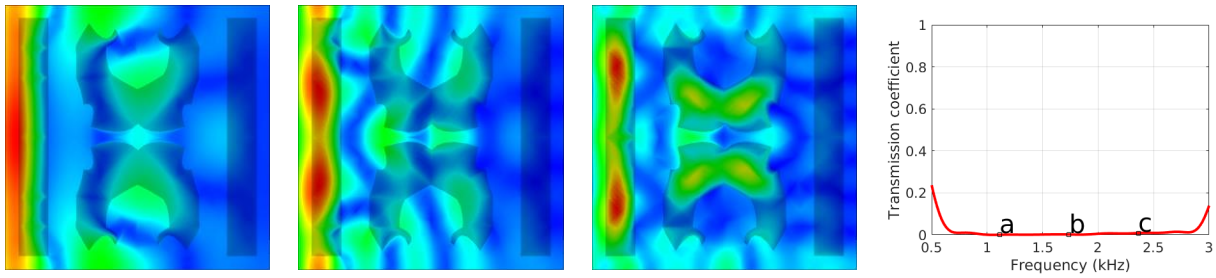

(a) (b) (c) (d)

Figure 4.32 Optimization results of case 3 with $\rho_e^2 = 8\rho_e^1$ and $K_e^2 = 8K_e^1$. Normalized pressure contours (blue-red: low-high) at (a) 1.1 kHz, (b) 1.75 kHz, (c) 2.4 kHz. (d) Transmission coefficient.

A shape optimization procedure is also conducted on a group of three dimensional cylinders to achieve the desired noise reductions. Again, the attenuation of the sound pressure downstream (+x direction) of the phononic crystals in a frequency range is chosen to be the design target, with ω_1 = 2.5 kHz and ω_2 = 3.0 kHz, and $\hat{p}$ is the

frequency domain solution.

The original cylindrical shapes are shown in Fig. 4.33, and the optimized distributions are given in Fig. 4.34. It can be seen that the cylinders tend to move towards both the upstream (-*x*) and downstream (+*x*) directions. Note that symmetry conditions are enforced in the transverse z direction where the periodic boundary conditions are applied. The transmission of the pressure is plotted against frequency in Fig. 4.35 for both the original and the optimal shapes. The black solid line represents the pressure with the original shape, and the red dashed line represents the one with the optimization. It is shown from this figure that the sound pressures at the target frequency range are effectively reduced by the shape optimization. However, it is also noticed that the noise transmission at lower frequencies is increased as a consequence.

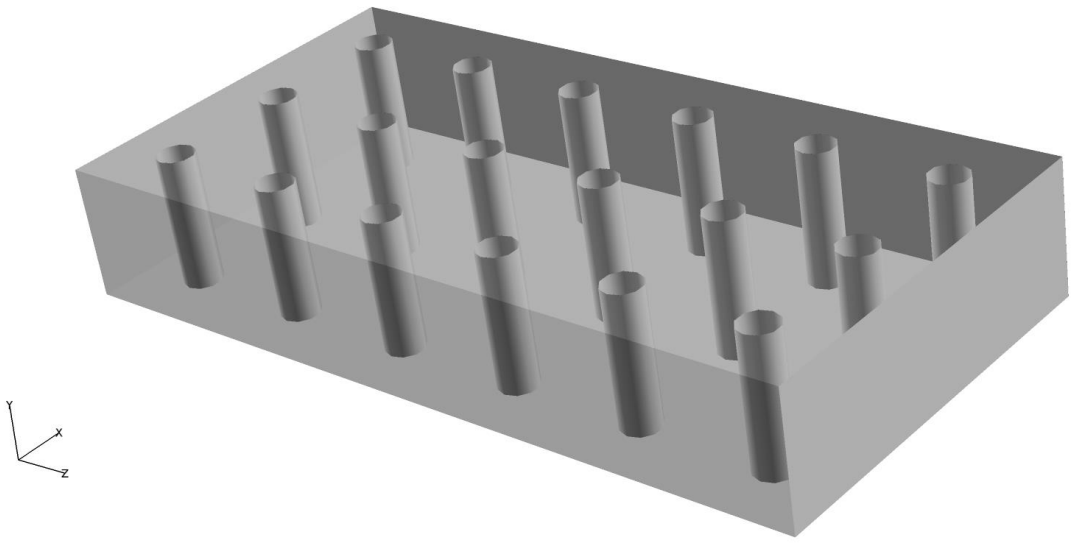

Figure 4.33 The original shapes of phononic crystals

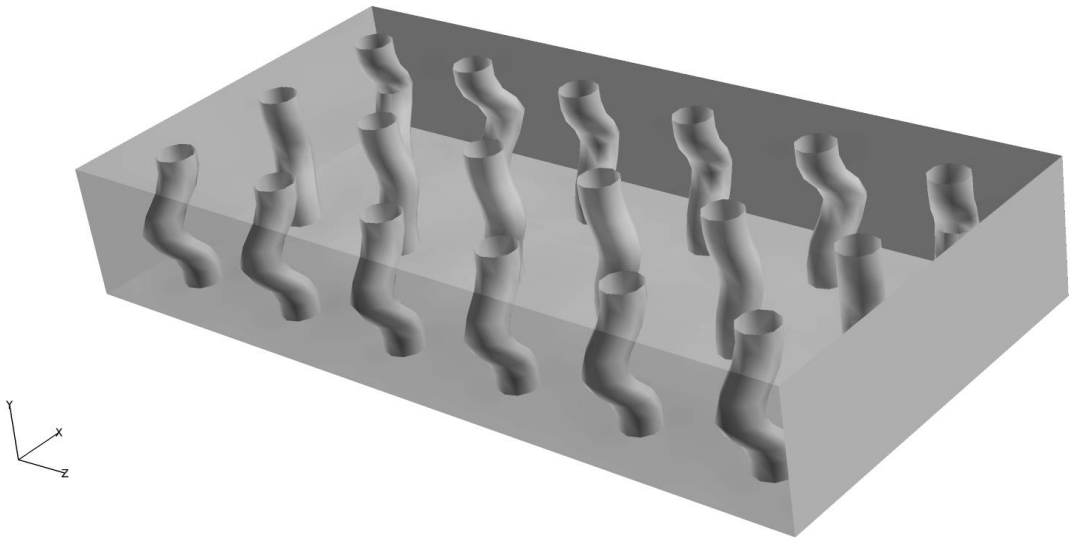

Figure 4.34 The optimal shapes of phononic crystals for noise reductions in the frequency range from 2.5 kHz to 3.0 kHz

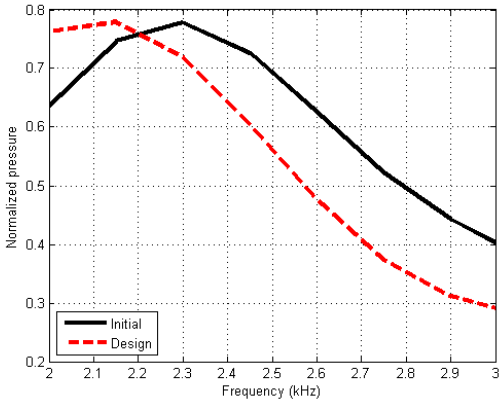

Figure 4.35 The transmissions of sound pressure at different frequencies.

CHAPTER 5

SUMMARY AND FUTURE WORK

In this dissertation, a time-dependent adjoint approach for obtaining sensitivity derivatives for shape optimizations of acoustic metamaterials and phononic crystals is presented. The acoustic wave propagation problem is solved in the time-domain using a Streamline Upwind/Petrov Galerkin formulation. Topology optimization is accomplished using the homogenization method, and shape optimization is subsequently used to fine tune the geometries. The combined strategy is compared with penalty-based topology optimization. Surface parameterization is accomplished using control grids, which are based on a Laplacian-type equation.

The gradient-based design procedure is suitable for large numbers of design variables. The proposed optimization framework is also utilized on the design of different acoustic materials. First, a broadband acoustic cloaking device is designed using the homogenization-based topology optimization. The scattered acoustic wave strength is minimized in the frequency range of 1.9 kHz to 2.1 kHz. Second, a sequential topology optimization method is carried out to design acoustic metamaterials and phononic crystals. The optimized acoustic metamaterials show the desired effective material properties, and the resulting phononic crystals show broadband noise reduction. The sequential method is shown to be more efficient than shape or topology optimization

only.

Several aspects of future work are suggested. First, extend the sensitivity analysis to the elastic solver. In this research, the proposed optimization framework is only implemented on the acoustic wave solver, which ignores S-wave when solids are present. Second, in order to simulate high frequency waves, higher order methods need to be implemented, and a dispersive acoustic wave equation should be considered in order to account for the acoustic power loss. In addition, more advanced numerical methods, such as space time algorithms, Krylov-based projections, are recommended to alleviate the computational burden of the current finite element time domain method.

REFERENCES

Alagoz, B Baykant, and Serkan Alagoz. 2009. 'Seismic crystals and earthquake shield application', *arXiv preprint arXiv:0902.1429*.

Allaire, Grégoire, and François Jouve. 2006. "Coupling the level set method and the topological gradient in structural optimization." In *IUTAM symposium on topological design optimization of structures, machines and materials*, 3-12. Springer.

Anderson, W Kyle, Steve L Karman, and Chad Burdyshaw. 2009. 'Geometry parameterization method for multidisciplinary applications', *AIAA journal*, 47: 1568-78.

Anderson, W Kyle, James C Newman, David L Whitfield, and Eric J Nielsen. 2001. 'Sensitivity analysis for Navier-Stokes equations on unstructured meshes using complex variables', *AIAA journal*, 39: 56-63.

Anderson, W Kyle, and V Venkatakrishnan. 1999. 'Aerodynamic design optimization on unstructured grids with a continuous adjoint formulation', *Computers & Fluids*, 28: 443-80.

Anderson, W Kyle, Li Wang, Sagar Kapadia, Craig Tanis, and Bruce Hilbert. 2011. 'Petrov–Galerkin and discontinuous-Galerkin methods for time-domain and frequency-domain electromagnetic simulations', *Journal of computational physics*, 230: 8360-85.

Andkjær, Jacob, and Ole Sigmund. 2013. 'Topology optimized cloak for airborne sound', *Journal of Vibration and Acoustics*, 135: 041011.

Bendsøe, Martin Philip, and Noboru Kikuchi. 1988. 'Generating optimal topologies in structural design using a homogenization method', *Computer methods in applied mechanics and engineering*, 71: 197-224.

Bonhaus, Daryl Lawrence. 1998. 'A higher order accurate finite element method for viscous compressible flows', *A higher order accurate finite element method for viscous compressible flows*.

Botteldooren, Dick. 1995. 'Finite ‐ difference time ‐ domain simulation of low ‐ frequency room acoustic problems', *The Journal of the Acoustical Society of America*, 98: 3302-08.

Brillouin, Leon. 2003. *Wave propagation in periodic structures: electric filters and crystal lattices* (Courier Corporation).

Brooks, Alexander N, and Thomas JR Hughes. 1982. 'Streamline upwind/Petrov-Galerkin formulations for convection dominated flows with particular emphasis on the incompressible Navier-Stokes equations', *Computer methods in applied mechanics and engineering*, 32: 199-259.

Chen, Huanyang, and CT Chan. 2007. 'Acoustic cloaking in three dimensions using acoustic metamaterials', *Applied physics letters*, 91: 183518.

Cockburn, Bernardo, and Chi-Wang Shu. 1998. 'The local discontinuous Galerkin method for time-dependent convection-diffusion systems', *SIAM Journal on Numerical Analysis*, 35: 2440-63.

Craster, Richard V, and Sébastien Guenneau. 2012. *Acoustic metamaterials: Negative refraction, imaging, lensing and cloaking* (Springer Science & Business Media).

Cummer, Steven A, Bogdan-Ioan Popa, David Schurig, David R Smith, and John Pendry. 2006. 'Full-wave simulations of electromagnetic cloaking structures', *Physical Review E*, 74: 036621.

Cummer, Steven A, and David Schurig. 2007. 'One path to acoustic cloaking', *New Journal of physics*, 9: 45.

Deymier, Pierre A. 2013. *Acoustic metamaterials and phononic crystals* (Springer Science & Business Media).

Diaz, Alejandro R, and Ole Sigmund. 2010. 'A topology optimization method for design of negative permeability metamaterials', *Structural and Multidisciplinary Optimization*, 41: 163-77.

Dumbser, Michael, and Martin Käser. 2006. 'An arbitrary high-order discontinuous Galerkin method for elastic waves on unstructured meshes—II. The three-dimensional isotropic case', *Geophysical Journal International*, 167: 319-36.

Fokin, Vladimir, Muralidhar Ambati, Cheng Sun, and Xiang Zhang. 2007. 'Method for retrieving effective properties of locally resonant acoustic metamaterials', *Physical review B*, 76: 144302.

García-Chocano, Victor Manuel, L Sanchis, A Díaz-Rubio, J Martínez-Pastor, F Cervera, R Llopis-Pontiveros, and J Sánchez-Dehesa. 2011. 'Acoustic cloak for airborne sound by inverse design', *Applied physics letters*, 99: 074102.

Glasby, Ryan S, Nicholas Burgess, Kyle Anderson, Li Wang, Dimitri J Mavriplis, and Steven R Allmaras. 2013. "Comparison of SU/PG and DG finite-element techniques for the compressible navier-stokes equations on anisotropic unstructured meshes." In *Proceedings of the 51st AIAA Aerospace Sciences Meeting Including the New Horizons Forum and Aerospace Exposition*. American Institute of Aeronautics and Astronautics.

Guenneau, Sébastien, Alexander Movchan, Gunnar Pétursson, and S Anantha Ramakrishna. 2007. 'Acoustic metamaterials for sound focusing and confinement', *New Journal of physics*, 9: 399.

Hicks, Raymond M, and Preston A Henne. 1978. 'Wing design by numerical optimization', *Journal of Aircraft*, 15: 407-12.

Joannopoulos, John D, Steven G Johnson, Joshua N Winn, and Robert D Meade. 2011. *Photonic crystals: molding the flow of light* (Princeton university press).

Kallivokas, Loukas F, and Jacobo Bielak. 1993. 'Time ‐ domain analysis of transient structural acoustics problems based on the finite element method and a novel absorbing boundary element', *The Journal of the Acoustical Society of America*, 94: 3480-92.

Karypis, George, and Vipin Kumar. 1995. 'METIS--unstructured graph partitioning and sparse matrix ordering system, version 2.0'.

Käser, Martin, and Michael Dumbser. 2006. 'An arbitrary high-order discontinuous Galerkin method for elastic waves on unstructured meshes—I. The two-dimensional isotropic case with external source terms', *Geophysical Journal International*, 166: 855-77.

LeVeque, Randall J. 2002. *Finite volume methods for hyperbolic problems* (Cambridge university press).

Lin, Weiyang, William K Anderson, James Newman, and Xueying Zhang. 2016. "Shape Optimization of Two-Dimensional Acoustic Metamaterials and Phononic Crystals with a Time-Dependent Adjoint Formulation." In *57th AIAA/ASCE/AHS/ASC Structures, Structural Dynamics, and Materials Conference*, AIAA Paper 2016-1908.

Lin, Weiyang, James C Newman III, and Kyle Anderson. 2016. "Design of Broadband Acoustic Cloak Using Topology Optimization." In *ASME IMECE Conference 2016*, IMECE2016-68135. Phoenix, AZ.

Lin, Weiyang, James Newman, William K Anderson, and Xueying Zhang. 2016a. "Broadband Shape and Topology Optimization of Acoustic Metamaterials and Phononic Crystals." In *17th AIAA/ISSMO Multidisciplinary Analysis and Optimization Conference. Washington, D.C.*, AIAA Paper 2016-3216.

Lin, Weiyang, James Newman, William K Anderson, and Xueying Zhang. 2016b. "Shape Optimization of Acoustic Metamaterials and Phononic Crystals with a Time-Dependent Adjoint Formulation: Extension to Three-Dimensions." In *17th AIAA/ISSMO Multidisciplinary Analysis and Optimization Conference. Washington, D.C.*, AIAA Paper 2016-3830.

Liu, Zhengyou, Xixiang Zhang, Yiwei Mao, YY Zhu, Zhiyu Yang, CT Chan, and Ping Sheng. 2000. 'Locally resonant sonic materials', *Science*, 289: 1734-36.

Mur, Gerrit. 1981. 'Absorbing boundary conditions for the finite-difference approximation of the time-domain electromagnetic-field equations', *IEEE transactions on Electromagnetic Compatibility*: 377-82.

Newman III, James C, Arthur C Taylor III, Richard W Barnwell, Perry A Newman, and Gene J-W Hou. 1999. 'Overview of sensitivity analysis and shape optimization for complex aerodynamic configurations', *Journal of Aircraft*, 36: 87-96.

Nielsen, Eric J, and Michael A Park. 2006. 'Using an adjoint approach to eliminate mesh sensitivities in computational design', *AIAA journal*, 44: 948-53.

Otomori, Masaki, Lirong Lu, Shinji Nishiwaki, Takayuki Yamada, Kazuhiro Izui, and Takashi Yamamoto. 2013. 'Level Set-based Topology Optimization of Acoustic Metamaterials'.

Pendry, John B, David Schurig, and David R Smith. 2006. 'Controlling electromagnetic fields', *Science*, 312: 1780-82.

Pendry, John Brian. 2000. 'Negative refraction makes a perfect lens', *Physical review letters*, 85: 3966.

Saad, Yousef. 2003. *Iterative methods for sparse linear systems* (Siam).

Saad, Yousef, and Martin H Schultz. 1986. 'GMRES: A generalized minimal residual algorithm for solving nonsymmetric linear systems', *SIAM Journal on scientific and statistical computing*, 7: 856-69.

Tam, Christopher KW, and Jay C Webb. 1993. 'Dispersion-relation-preserving finite difference schemes for computational acoustics', *Journal of computational physics*, 107: 262-81.

Wang, Li, and Dimitri J Mavriplis. 2009. 'Adjoint-based h–p adaptive discontinuous Galerkin methods for the 2D compressible Euler equations', *Journal of computational physics*, 228: 7643-61.

Wang, Zhi Jian. 2002. 'Spectral (finite) volume method for conservation laws on unstructured grids. basic formulation: Basic formulation', *Journal of computational physics*, 178: 210-51.

Yamaleev, Nail K, Boris Diskin, and Eric J Nielsen. 2010. 'Local-in-time adjoint-based method for design optimization of unsteady flows', *Journal of computational physics*, 229: 5394-407.

Zhang, Shu. 2010. 'Acoustic metamaterial design and applications', University of Illinois at Urbana-Champaign.

Zhang, Shu, Chunguang Xia, and Nicholas Fang. 2011. 'Broadband acoustic cloak for ultrasound waves', *Physical review letters*, 106: 024301.

VITA

Weiyang “Ryan” Lin was born in Rui'an, Zhejiang, China, to the parents of Zhenxiong Lin and Yuqian Huang. He is the fifth of five children, three older sisters and an older brother. He attended Shiyan Elementary and continued to Wansong Middle school and Rui’an High School in Rui’an, Zhejiang, China. After graduation, attended South China Agricultural University. Ryan earned the Bachelors of Science degree in July 2009 in Information and Computing Sciences under the supervision of Mingliang Fang, and received honors recognition. He joined the SimCenter and worked with Kidambi Sreenivas and Robert Webster for his Master’s degree from the University of Tennessee at Chattanooga in August, 2013. He stayed and completed his Ph.D. under the supervision of James Newman and Kyle Anderson in December, 2016, and received the Outstanding Graduate Student Award.